Numerical Heat Transfer-Part A (USA)

https://www.tandfonline.com/toc/unht20/current

Accepted March 6th 2024

NEURAL NETWORK AND THERMODYNAMIC OPTIMIZATION OF MAGNETIZED HYBRID NANOFLUID DISSIPATIVE RADIATIVE CONVECTIVE FLOW WITH ENERGY ACTIVATION

M. Ferdows[1]*, Muktadir Ahmed[1], M. A. Bhuiyan[2], O. Anwar Bég[3*], A.B. Çolak[4] and H.J. Leonard[3]

[1]Research Group of Fluid Flow Modeling and Simulation, Department of Applied Mathematics

University of Dhaka, Dhaka-1000, Bangladesh.

[2]Department of Physics, University of Dhaka, Dhaka-1000, Bangladesh.

[3]Multi-Physical Engineering Sciences Group, Mechanical Engineering Department, School of Science, Engineering and Environment (SEE), University of Salford, Manchester, UK.

[4]Department of Mechanical Engineering, Engineering Faculty, Nigde Omer Halisdemir University, 51240, Nigde, Turkey

***Corresponding author**: ferdows@du.ac.bd*

ABSTRACT

This article, motivated by hybrid magnetic coating manufacturing developments, utilizes a neural network-based computational program to study the dynamics of hybrid magnetic nanofluids with entropy generation. A new physico-chemo-mathematical model has been presented to simulate the hybrid magnetic nano-coating flow along a stretching surface to a porous medium with viscous heating. A Rosseland flux model is used for radiation heat transfer, and Darcy's model for the isotropic porous medium. The stretching sheet is porous and wall suction or injection are possible. A robust neural network has been deployed to optimize the physical parameters controlling transport characteristics of hybrid nanofluids. Specifically, 2 hybrid nanoparticle combination are addressed, namely graphite oxide (GO)-molybdenum disulfide (MoS_2) and copper (Cu)-silicon dioxide (SiO_2), both with engine oil as the base fluid. The dimensional boundary layer model is transformed via suitable scaling variables from a partial differential system into a dimensionless non-linear coupled ordinary differential system. The transformed boundary value problem is solved numerically with the BVP4C subroutine in the symbolic software MATLAB, which achieves exceptional accuracy. Validation with previous simpler studies is conducted and good correlation is obtained. The neural network optimization analysis which incorporates Bayesian regularization as the training algorithm. The Bejan entropy generation minimization (EGM) analysis shows that with increasing radiation parameter R_d, both entropy generation rate and Bejan number are increased. Furthermore, an elevation in Brinkman number Br leads to an upsurge in entropy generation rate and a downtrend in Bejan number. The numerical solution of the boundary value problem reveals that with increment in nanoparticle solid volume fraction φ_2, magnetic parameter M, inverse permeability parameter ϵ, surface injection parameter ($s < 0$), Eckert number Ec and radiation parameter R_d and with a decrement in suction parameter ($s > 0$) and Prandtl number Pr, there is a strong enhancement in temperature magnitude and thermal boundary layer thickness. With greater nanoparticle solid volume fraction φ_2, magnetic parameter M, inverse permeability parameter ϵ, suction parameter s and a reduction in thermal buoyancy parameter λ, strong flow deceleration is induced, and momentum boundary layer thickness is increased. Skin friction coefficient is substantially boosted with lower values of magnetic parameter M, inverse permeability parameter ϵ, suction parameter s and higher values of thermal buoyancy parameter λ. There is a significant decrement also computed in

Nusselt number with greater radiation parameter R_d. The simulations provide a good benchmark for future extensions which may consider non-Newtonian behaviour.

KEYWORDS: *Hybrid magnetic nanofluids; boundary layers; coating; neural network; thermodynamic optimization, wall mass flux, entropy generation, MATLAB BVP4C, Bayesian regularization, $Cu - SiO_2/engine\ oil$ hybrid nanofluid, Bejan number; radiative heat flux; Brinkman number.*

NOMENCLATURE

(x, y) Cartesian coordinate system	μ_f dynamic viscosity of the fluid
u, v velocity components along (x, y) directions	μ_{nf} dynamic viscosity of the nanofluid
U_w wall velocity	μ_{hnf} dynamic viscosity of the hybrid nanofluid
T fluid temperature	ϑ_f kinematic viscosity of the fluid
T_w wall temperature	ϑ_{nf} kinematic viscosity of the nanofluid
T_∞ ambient temperature	ϑ_{hnf} kinematic viscosity of the hybrid nanofluid
a, b, c constants	η transformed transverse coordinate
f dimensionless stream function	σ electrical conductivity
θ dimensionless temperature function	σ_f electrical conductivity of the fluid
q_r radiative heat flux	σ_{nf} electrical conductivity of the nanofluid
σ^* Stefan Boltzmann constant	σ_{hnf} electrical conductivity of the hybrid Nanofluid
B uniform magnetic field	$(\rho\beta)_f$ thermal expansion of the fluid
B_0 magnetic induction	$(\rho\beta)_{nf}$ thermal expansion of the nanofluid
K thermal slip factor	$(\rho\beta)_{hnf}$ thermal expansion of the hybrid nanofluid
β Thermal expansion coefficient	C_{f_x} skin friction coefficient along x directions
C_p specific heat at constant pressure	q_w heat flux
$(\rho C_p)_f$ heat capacitance of the fluid	Nu_x local Nusselt number
$(\rho C_p)_{hnf}$ heat capacitance of the hybrid nanofluid	τ_{wx} wall shear stress along x directions
k thermal conductivity	Pr Prandtl number
k_f thermal conductivity of the fluid	A parameter for unsteadiness
k_{nf} thermal conductivity of the nanofluid	R_d radiation parameter
k_{hnf} thermal conductivity of the hybrid nanofluid	λ thermal buoyancy parameter
φ_1, φ_2 volume fraction coefficients	M magnetic parameter
K^* mean absorption coefficient	ϵ inverse permeability parameter
ρ density of the fluid	Ec Eckert number
ψ dimensional stream function	Gr thermal Grashof number

S suction/injection parameter	Re_x local Reynolds number
N_g entropy generation rate	Be Bejan Number
Ω Dimensionless temperature difference	Br Brinkman number

1. INTRODUCTION

The thin layer of viscous fluid in close proximity to a solid surface, as a result of fluid flow along the surface, is called the *boundary layer* [1]. The fluid contact with the boundary causes it to come to a standstill and this is termed the classical no-slip condition in boundary-layer theory. As the distance from the boundary increases, the fluid velocity increases until it attains the maximum (free stream) value. The thin shear layer where velocity has not yet reached the external inviscid flow velocity constitutes the hydrodynamic or momentum boundary layer. When heat and mas transfer are also present, as frequently encountered in materials processing and industrial thermos-hydraulics operations, additional thermal and concentration (solutal) boundary layers are also present. Each has a distinct thickness and unique characteristics. Even a century after its introduction, Prandtl's boundary-layer theory (which applied to both laminar and turbulent flows) remains the cornerstone of modern fluid dynamics. It is the single most important framework ever developed for fluid mechanics analysis and has been verified experimentally showing excellent correlation with real phenomena. Originating in aircraft wing aerodynamics it has successfully infiltrated into practically every application of viscous flow ranging from coating deposition to blood flows. An important category of boundary-layer flows is encountered in manufacturing operations where coatings are extruded onto engineering components (substrates). When the substrate is stretching or moving (translating), very precise fabrication of coatings can be achieved. Crane [2] was the first to study the boundary layer flow induced by a linearly stretching sheet and obtained analytical solutions for the purely hydrodynamic problem. Lin and Shih [2] extended this methodology to study thermal convection laminar boundary layer flow along cylinders that are moving horizontally and vertically at a constant velocity. They discovered that it was not possible to obtain similarity solutions due to the influence of the cylinder curvature on the flow. Since then, many researchers [4-9] have continued to build upon Crane's work extending models to consider non-Newtonian effects, non-Fourier heat flux, hydromagnetics, thermo-solutal transport (coupled heat and mass transfer), wall transpiration, nonlinear (quadratic, exponential) stretching and many other aspects. Magyari and Keller [10] studied the boundary layer flow and heat transfer caused by an exponentially stretching sheet for Newtonian liquids. Ishak [11] investigated the magnetohydrodynamic (MHD) boundary layer flow from an exponentially shrinking sheet with radiative flux effects. All these investigations confirmed the marked modifications that are induced in momentum, heat and mass transfer behaviour with wall stretching (or shrinking) which are important in real materials synthesis applications.

In the past several decades, various unique approaches have been developed to enhance the rate of heat transfer and achieve different levels of thermal efficiency in industrial fluid dynamics. A key objective has been the sustainable and inexpensive improvement of thermal conductivity. Researchers have made significant efforts to disperse high thermal conducting solid particles into working liquids to achieve this goal. Fluids play a crucial role in thermal management systems, helping to regulate and improve the rate of heat transfer [12]. This is also of relevance in optimizing the manufacture of complex coatings [5] where thermal properties contribute significantly to the constitutional homogeneity of final products. With advancements in technology, the amount of heat output in modern systems has increased, requiring higher rates of heat transfer to prevent overheating. In 1995, researchers Choi [13] discovered that adding solid nanoparticles to fluids, known as *nanofluids*, can significantly increase their thermal conductivity [14]. Nanofluids are a novel category of fluids created by incorporating nanometer-sized materials (such as nanoparticles, nanofibers, nanotubes, nanowires, nanorods, nanosheets, or droplets) into a base fluid. Essentially, nanofluids are nanoscale suspensions composed of condensed nanomaterials. They are a two-phase colloidal suspension system, with one phase being a solid and the other a liquid. Nanofluids have become increasingly popular as working fluids due to their improved heat transfer capabilities although they also exhibit higher viscosity [15]. However, they have the key advantage of avoiding agglomeration (clustering) effects encountered in, for example, microscale particle-based fluids, which can lead to clogging, discontinuous distribution etc. In recent years, the study of nanofluids has attracted enormous attention both experimentally and theoretically. Early formulations developed to describe flows of nanofluids include the Tiwari-Das nanoscale model and the Buongiorno two-component model, both of which have been reviewed in detail by Bég [16]. The former model (Tiwari-Das) is useful for studying actual nanomaterials since it provides a framework for nano-particle volume fraction and includes momentum and energy equations but does not feature nanoparticle mass diffusion physics. The latter model (Buongiorno) does feature a formulation for nanoparticle mass diffusion but cannot be deployed for studying actual nanomaterial types as it excluded a volume fraction feature and has no relationships for nanoparticle properties. Kuznetsov and Nield [17] presented one of the first studies of natural convective boundary layer flow of nanofluids using the Buongiorno model, noting that smaller nanoparticle sizes correspond to stronger Brownian motion effects. The main driving force behind the research on nanofluids is their ever-widening range of potential applications which are being embraced in diverse areas including environmental contamination reduction, nano-drug delivery, solar collector optimization and emerging smart coating materials.

Several review articles have been presented on the progress of nanofluid research in recent years, often with a focus on experimental and theoretical studies of the thermophysical properties or convective heat transfer of unitary nanofluids [18-20]. Unitary nanofluids deploy a single nanoparticle material type. However, engineers have explored the idea of combining different nanoparticle types (and shapes) and have recently developed the hybrid nanofluid. A hybrid nanofluid is a homogeneous mixture of two or more nanoparticles that have formed new physical and chemical bonds. Binary hybrid nanofluids contain two nanoparticles, ternary contain three and so on. The main idea behind using hybrid nanofluids is to achieve a significant improvement in thermophysical, hydrodynamic and mass transfer properties when compared to traditional single component (unitary) nanofluids, due to the synergistic effect [21]. Niihara [22] presented a new material design concept for nanocomposites that improved mechanical and thermal properties. Jana [23] observed that, the addition of single and hybrid nano-additives further enhances successfully the thermal conductivity of fluids. This means that the ability of the fluid to transfer heat is increased when these nano-additives are added. Suresh [24] synthesized a $(Al_2O_3 - Cu/water)$ hybrid nanofluid, which showed significant improvements in thermal and mechanical properties. Additionally, Momin [25] examined mixed convection with $(Al_2O_3/water)$ hybrid nanofluid in an inclined tube for laminar flow. Suresh *et al.* [26] investigated the effect of $(Al_2O_3 - Cu/water)$ hybrid nanofluid in thermal engineering systems.

Magnetohydrodynamics (MHD) has a wide range of applications in modern materials processing, metallurgy, renewable energy systems, nuclear reactor technology etc. It involves the interaction of viscous electro-conductive fluids with externally applied magnetic fields. MHD flows have therefore been extensively studied in industrial systems including magnetic spin coating and stretching sheet dynamics. Nanofluids containing magnetic nanoparticles invoke MHD effects. Pattnaik *et al.* [27] computed the magnetic nanofluid enrobing coating boundary layer flow on a stretching cylinder with homogeneous/heterogeneous reactions using titania nanoparticles. Hybrid magnetic nanofluids e.g. $Al_2O_3 - Cu$ -water hybrid nanofluids on a stretching wall were considered by Usman *et al.* [28] with MHD and radiative flux. Further studies include Nayak *et al.* [29] (on hydromagnetic nanofluids from an extending porous wall), Khan *et al.* [30] (second law thermodynamic analysis of rotating channel hybrid nanofluid MHD flow), Reddy *et al.* [31] (perturbation analysis of MHD reactive nanofluid flow from a rotating wall), Samart *et al.* [32] (unsteady viscoplastic nanofluid transport with MHD and radiative flux) and Iqbal *et al.* [33] (on Hall current magnetized oscillating hybrid nanofluid flows). The studies considered many other phenomena discussed in conjunction with hybrid nanoparticle effects including multiple wall slip, bi-axial stretching and Coriolis body forces. The specific role of *wall stretching* has received significant attention not just in nanofluid dynamics but also non-Newtonian transport phenomena. Relevant studies have deployed a range of numerical methods including finite element methods, finite difference methods and shooting quadrature to solve the associated nonlinear partial differential and ordinary differential boundary value problems. Further investigations of both unitary and binary hybrid nanofluid dynamics have been presented in [34-39]. These investigations have shown that net shear stress and drag experienced by the nanofluid is enhanced as a result of lateral stretching. Grosan and Pop [40] generalized single direction stretching sheet nanofluid transport to the case of bi-directional stretching/shrinking with a modified nanoscale model.

Entropy generation analysis is a valuable method for enhancing the efficiency of thermal systems. Recent investigations have also shown that incorporating nanoparticles into the base fluid can impact the overall entropy generation in a system. Thermodynamic systems are susceptible to a number of phenomena that result in energy wastage. These may include diffusion, chemical reactions, drag between solid surfaces, and the internal resistance of fluids. These factors can all contribute to a rise in entropy, which can negatively affect the system performance. The optimization of entropy and the application of the *second law of thermodynamics* are crucial methods for systems in thermodynamics including coatings, power generation, thermal ducts, propulsion and heat exchangers. These techniques were first introduced by the Romanian-American mechanical engineer Bejan [41-42]. Now known as Bejan's entropy generation minimization (EGM) this approach has been deployed in multiple applications to accurately evaluate and improve the performance of thermodynamic systems by reducing entropy generation and increasing the net thermal efficiency. Sciacovelli [43] lucidly reviewed the various theoretical and practical applications of EGM in different engineering systems. Manjunath and Kaushik [44] applied EGM to heat exchangers. External coating flows with entropy generation were scrutinized by Reddy *et al.* [45] for a second order viscoelastic polymeric liquid with an optimized finite difference code. Gajjela *et al.* [46] computed the internal coating of a micropolar magnetic liquid with entropy generation. Thameem Basha *et al*. [47] studied the external coating of a horizontal cylinder with a magnetic shear-thinning nanofluid, computing the entropy generation and Bejan number over a wide range of thermal buoyancy parameter values with the Keller box method. Khan *et al.* [48] considered radiative heat transfer contributions to entropy generation in reacting nanofluids with activation energy effects. Further studies include Shukla *et al.* [49] (on time-dependent Hiemenz stagnation coating flow of a radiative magnetic nanofluid with chemical reaction and shape factor effects) and Reddy *et al.* [50] (on third grade viscoelastic non-Fourier magnetic nanofluid internal coating flows). All these investigations confirmed that EGM permits unique combinations of control parameters to be identified for strategically optimizing heat transfer efficiency and reducing entropy generation and losses.

In recent years, engineers have increasingly adopted artificial neural networks (ANNs) due to its effectiveness in accommodating large data sets generated in a wide range of complex multi-physical, multi-scale engineering applications. In the context of nanofluids, ANNs have been implemented in smart nanofluid magnetic biomimetic pumps [51], coating flows of nanofluids in porous media [52] and reactive nanofluid transport around bluff bodies [53]. These networks have been utilized for analysis, forecasting and optimization of thermal and other characteristics. For instance, researchers have applied ANNs to examine the distribution of temperature in a porous fin model [54], while others have employed a combination of ANNs and genetic algorithms to optimize the shape and angle of vortex generators and the volume fraction of nanoparticles in a flow in a rectangular channel [55]. Furthermore, various forms of ANNs, such as particle swarm optimization (PSO), artificial bee colony (ABC) and Support Vector Regression (SVR), can be considered a dependable and logical approach for predicting results [56]. Neural networks are widely used in current research due to their ability to provide solutions for a wide range of problems which involve non-linearity [57]. They are particularly useful for tasks such as extrapolation, noise robustness, interpolation and handling of insufficient data. Additionally, they are relatively easy to use and have a high degree of fault tolerance [58-59].

The focus of the present article is to deploy ANNs and EGM to conduct a neural network-based simulation with Bejan entropy generation minimization (EGM) hybrid magnetic nano-coating flow along a stretching surface to a porous medium with viscous dissipation. Specifically, 2 hybrid nanoparticle combination are examined, namely magnetic graphite oxide (GO)-molybdenum disulfide (MoS_2) and copper (Cu)-silicon dioxide (SiO_2), both with engine oil as the base fluid, which are appropriate for advanced smart polymeric nano-coatings. The novelty of the present study is therefore the combined approach with ANNs and EGM for these unique hybrid nanoparticle combinations which has not been addressed before in the literature. A new physico-chemo-mathematical boundary layer model has been presented to simulate the coating problem. Optically thick properties are assumed for the magnetic nanofluid, and the Rosseland diffusion flux model is deployed for radiation heat transfer. The Darcy model for the isotropic porous homogenous medium. The stretching sheet is porous and both wall suction or injection are examined. A robust neural network is deployed which incorporates Bayesian regularization as the training algorithm, to optimize the physical parameters controlling transport characteristics of hybrid nanofluids. The dimensional boundary layer model is transformed via suitable scaling variables from a partial differential system into a dimensionless non-linear coupled ordinary differential system. The transformed boundary value problem is solved numerically with the BVP4C subroutine in the symbolic software MATLAB which achieves exceptional accuracy. Validation with previous simpler studies is conducted. Extensive visualization of velocity, temperature, Nusselt number, skin friction, entropy generation rate, Bejan number, ANN epochs and other results are included. The simulations provide a good insight into thermal optimization of hybrid smart magnetic nano-coatings. The research applications also include enhancing heat transfer in energy systems, optimizing industrial processes, aiding biomedical multi-functional coating deposition and improving electromagnetic sensor surface design. Understanding convective flows, radiative heat transfer and magnetized nanofluids contributes to efficiency, performance and sustainability across various fields, including energy, manufacturing, healthcare and environmental science.

2. PHYSICAL MODEL AND MATHEMATICAL FORMULATION

In this work, we examine the two-dimensional unsteady magnetohydrodynamic (MHD) natural convection flow of a viscous and incompressible hybrid electrically conducting nanofluid in the presence of convective boundary conditions, from a stretching sheet embedded in a Darcian porous medium. The flow domain and the coordinate system are depicted in **Fig. 1**, where the *x and y* coordinates are directed along and perpendicular to the sheet. The stretching wall is porous and lateral mass flux arises (suction, injection). Viscous heating is included. The magnetic hybrid nanofluid is assumed to have uniform particle size, and we ignore agglomeration effects on thermophysical properties, assuming they are synthesized as a stable mixture of nanoparticles and base fluid. We have considered silicon dioxide (SiO_2), molybdenum disulfide (MoS_2), Graphite oxide (GO), Copper (Cu) as nanoparticles and engine oil as base fluid (polymeric nanocoating). Thermophysical properties are assumed to be constant. Rosseland's diffusion algebraic model is implemented for radiative heat flux. Magnetic induction is ignored since magnetic Reynolds number is sufficiently small. The sheet is electrically insulated, and Hall current effects are negated.

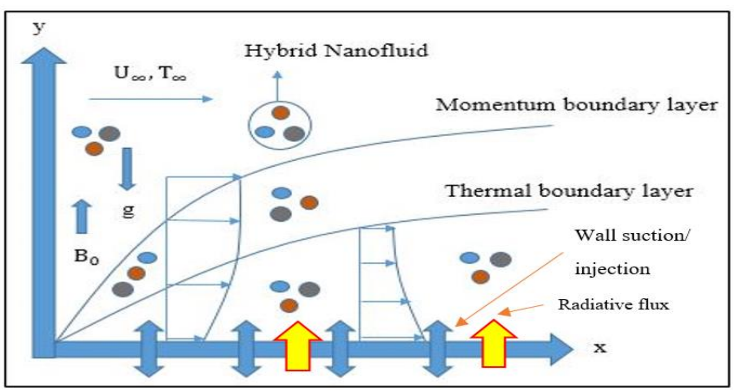

Figure 1: Physical configuration and coordinate system

Based on the above assumptions and under the usual boundary layer and Boussinesq approximations in $(x,\ y)$ coordinate system for the two-dimensional hybrid nanofluid are the governing continuity, momentum, and energy equations may be formulated by extending the models in [60-61]:

$$\frac{\partial u}{\partial x}+\frac{\partial v}{\partial y}=0 \tag{1}$$

$$\frac{\partial u}{\partial t}+u\frac{\partial u}{\partial x}+v\frac{\partial u}{\partial y}=\vartheta_{hnf}\left(\frac{\partial^2 u}{\partial y^2}-\frac{u}{K}\right)-\frac{\sigma_{hnf}}{\rho_{hnf}}B^2(t)u+\frac{g(\rho\beta)_{hnf}}{\rho_{hnf}}(T-T_\infty) \tag{2}$$

$$\frac{\partial T}{\partial t}+u\frac{\partial T}{\partial x}+v\frac{\partial T}{\partial y}=\frac{1}{(\rho C_p)_{hnf}}\left[K_{hnf}\frac{\partial^2 T}{\partial y^2}-\frac{\partial q_r}{\partial y}+\mu_{hnf}\left(\frac{\partial u}{\partial y}\right)^2\right] \tag{3}$$

Here *u* and *v* are velocity components in the *x* and *y*-directions, *t* is time, ϑ_{hnf} is kinematic viscosity of the hybrid magnetic nanofluid, K is permeability of the porous medium, σ_{hnf} is electrical conductivity, ρ_{hnf} is density, *B(t)* is magnetic field, β is coefficient of thermal expansion, *g* is gravitational acceleration, *T* is temperature, T_∞ is free stream temperature, *Cp* is specific heat capacity at constant pressure, K_{hnf} is thermal conductivity, c_p is its specific heat, μ_{hnf} is dynamic viscosity and q_r is the radiative heat flux. The velocity and temperature at the wall and in the free stream are specified with the following boundary conditions.

$$At\ y=0:\quad u=U_w,\ v=v_w,\ T=T_w,\ v_w=-\sqrt{\frac{\vartheta_f U_w}{x}}f(0)$$

$$At\ y\to\infty:\quad u\to 0,\ T\to T_\infty \tag{4}$$

The radiative heat flux (q_r) in Eqn. (3) is analyzed using the Rosseland flux model [49] as:

$$q_r=-\frac{4\sigma^*}{3K^*}\frac{\partial T^4}{\partial y} \tag{5}$$

Here σ^* is the famous Stefan-Boltzmann constant and K^* is the radiation extinction coefficient. The radiative heat flux can be approximated by linearizing via a Taylor series expansion, expanding T^4 about T_∞ then ignoring higher order terms. This yields the expression, $T^4 \cong 4T_\infty^3\,T-3T_\infty^3$.

2.1 Transformation of mathematical model

We employ the following transformations to non-dimensionalize Eqns. (1) to (4) [60-61],

$$\eta = \sqrt{\frac{U_w}{\vartheta_f x}}y, \qquad \psi = \sqrt{\vartheta_f x U_w} f(\eta),$$

$$u = \frac{ax}{1-ct} f'(\eta), \qquad v = -\sqrt{\frac{\vartheta_f a}{1-ct}}\, f(\eta), \;\; \theta(\eta) = \frac{T - T_\infty}{T_w - T_\infty} \tag{6}$$

Here, η is transformed transverse coordinate, ψ is dimensional stream function, $f\ (\eta)$ is the dimensionless stream function, U_w is the wall velocity, a and c are arbitrary constants, θ is the dimensionless temperature function and T_w is the wall temperature. By utilizing the scaling transformations in Eqn. (6) on the primitive conservation Eqn. (1-3) with the modified Rosseland flux term (5), the continuity eqn. (1) is automatically satisfied (via the Cauchy-Riemann equations), and the partial differential boundary value problem reduces to the following coupled non-dimensional ordinary differential momentum and thermal boundary layer equations:

$$\frac{\vartheta_{hnf}}{\vartheta_f}\{f'''(\eta) - \epsilon f'(\eta)\} + f(\eta)f''(\eta) - \{f'(\eta)\}^2 - A\left\{f'(\eta) + \frac{\eta}{2}f''(\eta)\right\} - \frac{\sigma_{hnf}/\sigma_f}{\rho_{hnf}/\rho_f} M f'(\eta) + \frac{(\rho\beta)_{hnf}/(\rho\beta)_f}{\rho_{hnf}/\rho_f}\lambda\theta(\eta) = 0 \tag{7}$$

$$\frac{1}{Pr \times \left\{(\rho C_p)_{hnf}/(\rho C_p)_f\right\}}\left\{\frac{K_{hnf}}{K_f} + \frac{4}{3}R_d\right\}\theta''(\eta) + \frac{\mu_{hnf}/\mu_f}{\left(\rho C_p\right)_{hnf}/\left(\rho C_p\right)_f} Ec\{f''(\eta)\}^2 - A\left\{\theta(\eta) + \frac{\eta}{2}\theta'^{(\eta)}\right\} - f'(\eta)\theta(\eta) + f(\eta)\theta'(\eta) = 0 \tag{8}$$

The corresponding boundary conditions at the sheet and in the free stream (4) emerge as follows:

$$f'(0) = 1, f(0) = s, \theta(0) = 1 \; at \; \eta = 0,$$

$$f'(\infty) \to 0,\; \theta(\infty) \to 0 \; at \; \eta = \infty. \tag{9}$$

Here the following dimensionless parameters arise:

Unsteadiness parameter, $A = \frac{c}{a}$, Prandtl number, $Pr = \frac{\vartheta_f (\rho C_p)_f}{K_f}$, Radiation parameter (Boltzmann number), $R_d = \frac{4\sigma^* T_\infty^3}{K^* K_f}$, Magnetic parameter, $M = \frac{\sigma_f B_0^2}{\rho_f a}$, Inverse permeability parameter, $\epsilon =$

$\frac{\vartheta_f(1-ct)}{aK}$, Eckert number, $Ec = \frac{U_w^2}{(C_p)_f(T_w-T_\infty)}$, Thermal buoyancy parameter, $\lambda = \frac{Gr}{Re_x^2}$, Thermal Grashof number, $Gr = \frac{g\beta_f(T_w-T_\infty)x^3}{\vartheta_f^2}$, Local Reynolds number, $Re_x = \frac{U_w x}{\vartheta_f}$.

(10)

2.2 Physical quantities of interest:

Important characteristics at the wall (sheet) in materials coating operations are the non-dimensional shear stress and heat transfer gradient (Nusselt number). These are formulated for the present problem as follows:

Skin friction component C_f along the $x-$ direction:

$$\therefore \frac{1}{2} C_f \sqrt{Re_x} = \frac{\mu_{hnf}}{\mu_f} f''(0) \tag{11}$$

The local Nusselt number:

$$\therefore \frac{Nu_x}{\sqrt{Re_x}} = -\frac{K_{hnf}}{K_f}\theta'(0) \tag{12}$$

2.3 Thermophysical Characteristics of Hybrid Nanofluid

The appropriate relations for both unitary and hybrid (binary) nanofluids used to compute dynamic viscosity, density, heat capacity, thermal expansion coefficient, thermal conductivity and electrical conductivity are given in **Table 1** following [62,63]. The computed values based on these relations are documented in **Table 2**.

Table 1: Thermophysical characteristics of nanofluid and hybrid nanofluid [62-63]

Thermophysical characteristics	***Nanofluid***	***Hybrid Nanofluid***
Dynamic viscosity	$\mu_{nf} = \frac{\mu_f}{(1-\varphi_1)^{2.5}}$	$\mu_{hnf} = \frac{\mu_f}{(1-\varphi_1)^{2.5}(1-\varphi_2)^{2.5}}$
Density	$\rho_{nf} = (1-\varphi_1)\rho_f + \varphi_1\rho_{s1}$	$\rho_{hnf} = (1-\varphi_2)\left[(1-\varphi_1)\rho_f + \varphi_1\rho_{s1}\right] + \varphi_2\rho_{s2}$

Heat capacity	$(\rho C_p)_{nf} = (1-\varphi_1)(\rho C_p)_f + \varphi_1(\rho C_p)_{s1}$	$(\rho C_p)_{hnf} = (1-\varphi_2)[(1-\varphi_1)(\rho C_p)_f + \varphi_1(\rho C_p)_{s1}] + \varphi_2(\rho C_p)_{s2}$
Thermal Expansion	$(\rho\beta)_{nf} = (1-\varphi_1)(\rho\beta)_f + \varphi_1(\rho\beta)_{s1}$	$(\rho\beta)_{hnf} = (1-\varphi_2)[(1-\varphi_1)(\rho\beta)_f + \varphi_1(\rho\beta)_{s1}] + \varphi_2(\rho\beta)_{s2}$
Thermal conductivity	$\frac{k_{nf}}{k_f} = \frac{k_{s1}+2k_f-2\varphi_1(k_f-k_{s1})}{k_{s1}+2k_f+\varphi_1(k_f-k_{s1})}$	$\frac{k_{hnf}}{k_{nf}} = \frac{k_{s2}+2k_{nf}-2\varphi_2(k_{nf}-k_{s2})}{k_{s2}+2k_{nf}+\varphi_2(k_{nf}-k_{s2})}$
Electrical conductivity	$\frac{\sigma_{nf}}{\sigma_f} = \frac{\sigma_{s1}+2\sigma_f-2\varphi_1(\sigma_f-\sigma_{s1})}{\sigma_{s1}+2\sigma_f+\varphi_1(\sigma_f-\sigma_{s1})}$	$\frac{\sigma_{hnf}}{\sigma_{nf}} = \frac{\sigma_{s2}+2\sigma_{nf}-2\varphi_2(\sigma_{nf}-\sigma_{s2})}{\sigma_{s2}+2\sigma_{nf}+\varphi_2(\sigma_{nf}-\sigma_{s2})}$

Table 2: Thermophysical characteristics [64-65]

Properties	Graphite oxide (GO)	Molybdenum disulfide (MoS_2)	Copper (Cu)	Silicon dioxide (SiO_2)	engine oil
Density $\rho(kg/m^3)$	1800	5060	8933	2650	884
Specific heat $c_p(J/KgK)$	717	397.21	385	730	1910
Thermal conductivity $k(W/mK)$	5000	904.4	400	1.5	0.144
Thermal expansion coefficient $\beta(1/K)$	0.284×10^{-5}	2.8424×10^{-5}	1.67×10^{-5}	0.55×10^{-6}	70×10^{-5}
Electrical Conductivity $\sigma(S/m)$	10^7	2.1×10^{-4}	5.96×10^7	10^{-25}	2.1×10^{-12}

3. ENTROPY GENERATION MINIMIZATION (EGM)

Entropy generation refers to the amount of energy that is lost or dissipated as a result of a process, which can lead to a decrease in the effectiveness of engineering systems such as conduction and convective heat transfer rate. Entropy measures the randomness of molecular behavior in a microscopic system. Heat drives thermodynamic irreversibility and entropy increases according to the second law of thermodynamics, which states that the entropy of a closed system never decreases. The system moves towards the maximum entropy equilibrium configuration. Entropy generation signifies a decline in energy quality and is crucial in heat transfer analysis. The presence of thermal radiation, porous medium fibers, viscous heating and variations in thermal conductivity as featured in the present hybrid magnetic nanofluid coating model, are all factors that contribute to different types of irreversibility in the flow and thermal gradients.

The *local volumetric rate of entropy generation* $S_{gen}(W/m^3K)$ is given as [66-67]:

$$\begin{aligned}
S_{gen} &= \frac{K_f}{T_\infty^2}\left(\frac{K_{hnf}}{K_f}+\frac{4}{3}R_d\right)\left(\frac{\partial T}{\partial y}\right)^2+\frac{\mu_{hnf}}{T_\infty}\left(\frac{\partial u}{\partial y}\right)^2 \qquad (13)\\
&= \frac{K_f}{T_\infty^2}\left(\frac{K_{hnf}}{K_f}+\frac{4}{3}R_d\right)(T_w-T_\infty)^2\frac{a}{\vartheta_f(1-ct)}\{\theta'(\eta)\}^2+\frac{\mu_{hnf}}{T_\infty}\frac{a^3x^2}{\vartheta_f(1-ct)^3}\{f''(\eta)\}^2\\
&= \frac{K_f(T_w-T_\infty)^2}{T_\infty^2}\frac{a}{\vartheta_f(1-ct)}\left\{\left(\frac{K_{hnf}}{K_f}+\frac{4}{3}R_d\right)\{\theta'(\eta)\}^2+\frac{\mu_{hnf}}{\mu_f}\cdot\frac{T_\infty}{T_w-T_\infty}\right.\\
&\qquad\left.\cdot\frac{\mu_f U_w^2}{K_f(T_w-T_\infty)}\{f''(\eta)\}^2\right\}\\
&= \frac{K_f(T_w-T_\infty)^2}{T_\infty^2}\frac{a}{\vartheta_f(1-ct)}\left\{\left(\frac{K_{hnf}}{K_f}+\frac{4}{3}R_d\right)\{\theta'(\eta)\}^2+\frac{\mu_{hnf}}{\mu_f}\cdot\frac{Br}{\Omega}\{f''(\eta)\}^2\right\}
\end{aligned}$$

The first term on the right-hand side of Eq. (12) represents *irreversibility due to heat transfer* and the second term represents *irreversibility due to viscous dissipation (internal friction in the nanofluid)*.

The characteristic entropy generation is defined as [66-67]:

$$(S_{gen})_0 = \frac{K_f(T_w-T_\infty)^2}{T_\infty^2 x^2} \qquad (14)$$

Next, the *local entropy generation rate* is given by,

$$\begin{aligned}
N_g &= \frac{S_{gen}}{(S_{gen})_0}\\
&= \frac{K_f(T_w-T_\infty)^2}{T_\infty^2}\frac{a}{\vartheta_f(1-ct)}\frac{T_\infty^2x^2}{K_f(T_w-T_\infty)^2}\left\{\left(\frac{K_{hnf}}{K_f}+\frac{4}{3}R_d\right)\{\theta'(\eta)\}^2+\frac{\mu_{hnf}}{\mu_f}\cdot\frac{Br}{\Omega}\{f''(\eta)\}^2\right\}\\
&= \frac{ax^2}{\vartheta_f(1-ct)}\left[\left(\frac{K_{hnf}}{K_f}+\frac{4}{3}R_d\right)\{\theta'(\eta)\}^2+\frac{\mu_{hnf}}{\mu_f}\cdot\frac{Br}{\Omega}\{f''(\eta)\}^2\right]
\end{aligned}$$

$$= \frac{U_w x}{\vartheta_f}\left[\left(\frac{K_{hnf}}{K_f} + \frac{4}{3}R_d\right)\{\theta'(\eta)\}^2 + \frac{\mu_{hnf}}{\mu_f}\cdot\frac{Br}{\Omega}\{f''(\eta)\}^2\right]$$

$$= Re_x\left[\left(\frac{K_{hnf}}{K_f} + \frac{4}{3}R_d\right)\{\theta'(\eta)\}^2 + \frac{\mu_{hnf}}{\mu_f}\cdot\frac{Br}{\Omega}\{f''(\eta)\}^2\right] \quad (15)$$

Here Brinkman number, $Br = \frac{\mu_f U_w^2}{K_f(T_w - T_\infty)}$ and dimensionless temperature difference, $\Omega = \frac{(T_w - T_\infty)}{T_\infty}$.

In the case of entropy generation minimization, the objective function may involve minimizing the total entropy generation rate or minimizing specific entropy generation terms within the system. The optimal solution obtained from the optimization process can be implemented in the design or operation of the thermodynamic system to achieve improved efficiency, reduced energy consumption and other desired outcomes.

3.1 Bejan Number

In thermal systems, Bejan number close to 1 indicates that *thermal* entropy generation is more dominant than *frictional* entropy generation in the overall entropy production. For $Be < 0.5$ the entropy generation produced by energy dissipation exceeds by that due to heat transfer. Bejan number can be defined following [66] as:

$$Be = \frac{\text{Entropy production due to thermal irreversibility}}{\text{Total entropy generation}}$$

$$= \frac{Re_x\left[\left(\frac{K_{hnf}}{K_f} + \frac{4}{3}R_d\right)\{\theta'(\eta)\}^2\right]}{Re_x\left[\left(\frac{K_{hnf}}{K_f} + \frac{4}{3}R_d\right)\{\theta'(\eta)\}^2 + \frac{\mu_{hnf}}{\mu_f}\cdot\frac{Br}{\Omega}\{f''(\eta)\}^2\right]}$$

$$= \frac{\left(\frac{K_{hnf}}{K_f} + \frac{4}{3}R_d\right)\{\theta'(\eta)\}^2}{\left(\frac{K_{hnf}}{K_f} + \frac{4}{3}R_d\right)\{\theta'(\eta)\}^2 + \frac{\mu_{hnf}}{\mu_f}\cdot\frac{Br}{\Omega}\{f''(\eta)\}^2} \quad (16)$$

4. NUMERICAL SOLUTION OF BOUNDARY VALUE PROBLEM AND VALIDATION

Computational solutions to the derived ordinary differential boundary value problem i. e. Eqns. (7), (8) and boundary conditions (9) are calculated by using the bvp4c solver, which implements a numerical method called 3-stage Lobatto IIIa collocation [68]. This method belongs to the finite difference discretization family of techniques. To use the bvp4c solver, the nonlinear ordinary differential equations and boundary conditions in Eqs. (7) to (8) need to be reformulated and the basic syntax used is sol = bvp4c (@OdeBVP, @OdeBC, solinit). This leads to the reduced system:

$$f = y(1)$$
$$f' = y(2)$$
$$f'' = y(3)$$
$$f''' = \epsilon f'(\eta) + \frac{\vartheta_{hnf}}{\vartheta_f}\left[\{f'(\eta)\}^2 - f(\eta)f''(\eta) + A\left\{f'(\eta) + \frac{\eta}{2}f''(\eta)\right\} + \frac{\sigma_{hnf}/\sigma_f}{\rho_{hnf}/\rho_f}Mf'(\eta) - \frac{(\rho\beta)_{hnf}/(\rho\beta)_f}{\rho_{hnf}/\rho_f}\lambda\theta(\eta)\right]$$
$$\theta = y(4)$$
$$\theta' = y(5)$$
$$\theta'' = \frac{Pr \times \{(\rho C_p)_{hnf}/(\rho C_p)_f\}}{\left\{\frac{K_{hnf}}{K_f} + \frac{4}{3}R_d\right\}}\left[A\left\{\theta(\eta) + \frac{\eta}{2}\theta'(\eta)\right\} - \frac{\mu_{hnf}/\mu_f}{\left(\rho C_p\right)_{hnf}/\left(\rho C_p\right)_f}Ec\{f''(\eta)\}^2 + f'(\eta)\theta(\eta) - f(\eta)\theta'(\eta)\right]$$

(17a-g)

These equations are coded into the function @OdeBVP.

The boundary conditions are formulated as:

$$ya(1) = s, ya(2) = 1, ya(4) = 1, \qquad (18)$$
$$yb(2) = yb(4) = 0$$

In the above statement, "ya" and "yb" refer to the initial and boundary conditions, respectively. These conditions are specified in the @OdeBC function. The "solininit" function contains the initial mesh points and initial guesses at these points. Multiple solutions can be obtained by providing additional initial guesses in the solinit function. The step size of $\Delta\eta = 0.05$ was selected to meet the convergence criteria of 10^{-5} in all cases. The value of η_∞ was determined for each iteration loop by adding $\Delta\eta$ to the previous value, i. e. $\eta_\infty = \eta_\infty + \Delta\eta$. The numerical MATLAB results (bvp4c) are first validated with viscous fluid i. e. in the absence of either hybrid nanoparticle

$(\varphi_1 = \varphi_2 = 0)$ without unsteadiness, dissipation, porous medium, magnetic, radiative, thermal buoyancy or wall mass flux effects $(A = Ec = \epsilon = M = R_d = \lambda = s = 0)$ based on previous solutions in the existing literature for Nusselt number. The comparisons are presented in **Table 3** and very good agreement is achieved confirming the accuracy of the current MATLAB bvp4c results.

Table 3: Comparison results for heat transfer rate $-\theta'(0)$ for various Prandtl numbers with $A = Ec = \epsilon = M = R_d = \lambda = s = \varphi_1 = \varphi_2 = 0$.

Pr	Jamshed *et al* [72]	Nisar *et al* [74]	Jamshed *et al* [75]	Present MATLAB bvp4c
1	1.0	1.0	1.0	1.0
3	1.923574	1.923574	1.923574	1.919243
7	3.073146	3.073146	3.073146	3.069175
10	3.720554	3.720554	3.720554	3.719087

5. NEURAL NETWORK OPTIMIZATION

Artificial intelligence (AI) refers to the development of intelligent computer systems that can perform tasks that typically require human intelligence, such as speech recognition, decision-making and visual perception. AI uses algorithms and statistical models to analyze data and make predictions or decisions based on that analysis. There are several branches of AI, including machine learning, deep learning, natural language processing, computer vision, robotics, and expert systems. Machine learning, in particular, focuses on the development of algorithms that can learn from and make predictions on data without being explicitly programmed. Artificial Neural Networks (ANNs) are a type of computational model that draw inspiration from the structure and function of biological nervous systems. One of the most commonly used forms of ANNs is the Multi-Layer Perceptron (MLP). The MLP is made up of three main layers: input, hidden, and output. The structure of MLP represent in **Figure 2**. This approach is implemented in the present study.

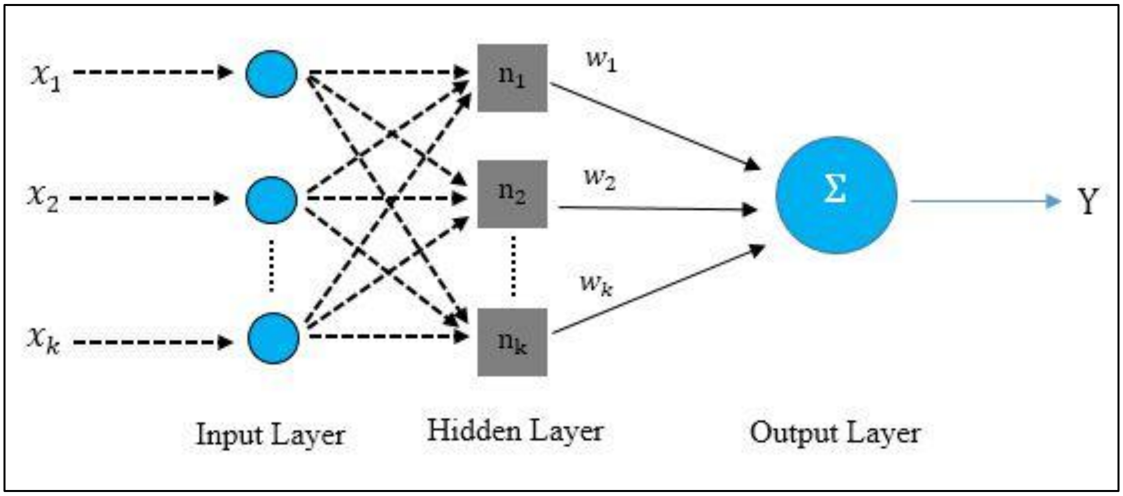

Figure 2: Structure of Multi-layer Perceptron in the ANN

The number of hidden layers can vary based on the complexity of the problem and the amount of data noise. Each node in the MLP is connected to the nodes in the next layer by means of a weight vector. The inputs are summed up in the first layer and then passed on as inputs to the next layer. The output of the b_j node in the next layer is determined by the input n_j, the weight in the connection and the threshold of the b_j node.

$$n_j = \sum_{i=1}^{n} w_{ji} x_i + b_j, \qquad b_j = 1, 2, \ldots, K \tag{19}$$

The inputs are then transformed by a *transfer function*, which gives the overall inputs to the next layer. The outputs of the hidden layer are then multiplied by the corresponding linking weights to obtain the final node output. The size and number of hidden layers can vary based on the problem, but there is no standard method for determining these parameters. To create predictive models using MLP, a *training stage* is necessary. This stage adjusts the bias and weight values through the use of algorithms such as backpropagation. The training process adds neurons incrementally until an optimal solution is reached. To utilize the ANN approach, data has to be first generated from the MATLAB numerical solutions. This stage is described first. Next, we address the ANN computations based on this generated data.

5.1 MATLAB data generated

Table 4 compares the influence of various different parameters on the skin friction coefficient for $GO - MoS_2/EO$ and $Cu - SiO_2/EO$ hybrid nanofluids. It is evident that with increasing inverse permeability parameter *(ε)*, magnetic parameter *(M)* and unsteadiness parameter *(A)*, the skin friction coefficient is decreased. However, with increasing thermal buoyancy parameter, the skin friction coefficient is increased. In all cases, $GO - MoS_2/EO$ consistently achieves a higher skin friction coefficient than $Cu - SiO_2/EO$.

Table 4: Effect of various parameters on skin friction for $GO - MoS_2/EO$ and $Cu - SiO_2/EO$.

ϵ	λ	M	A	Skin Friction(C_{fx})	
				$GO - MoS_2/EO$	$Cu - SiO_2/EO$
0.5	0.5	2	1	-2.2472	-2.3751
1				-2.3635	-2.4917
1.5				-2.4739	-2.6024
0.5	-0.5	2	1	-2.2961	-2.4025
	0			-2.2717	-2.3888
	0.5			-2.2472	-2.3751
0.5	0.5	1	1	-1.9391	-2.2040
		2		-2.2472	-2.3751
		3		-2.5155	-2.5330
0.5	0.5	2	-0.5	-2.0112	-1.9785
			0.5	-2.1705	-2.2477
			1	-2.2472	-2.3751

Table 5: Effect of various parameters on Nusselt number for $GO - MoS_2/EO$ and $Cu - SiO_2/EO$.

Pr	R_d	Ec	Nusselt number (Nu_x)	
			$GO - MoS_2/EO$	$Cu - SiO_2/EO$
30	0.4	0.01	9.4191	10.3746
40			11.7474	12.9791
50			14.0030	15.5090
50	0.2	0.01	15.8004	17.5445
	0.4		14.0030	15.5090
	0.6		12.6263	13.9551
50	0.4	0.001	14.2062	15.7242
		0.005	14.1159	15.6285
		0.01	14.0030	15.5090

Table 5 compares the impact of different selected parameters on Nusselt number for $GO - MoS_2/EO$ and $Cu - SiO_2/EO$. Evidently with increasing Prandtl number, *Pr*, (decreasing thermal conductivity) the heat transfer rate is also increased since the nanofluid in the boundary layer will be cooled and the net heat transfer to the wall be boosted. However, with increasing radiation

parameter *(Rd)* and Eckert number *(Ec)*, the heat transfer rate is decreased. Higher radiative flux and viscous heating will energize the nanofluid within the boundary layer and elevated temperatures. This will produce a concomitant reduction in heat diffusing to the wall and therefore lower Nusselt numbers. $\mathrm{Cu}-\mathrm{SiO_2/EO}$ exhibits higher heat transfer rates than $\mathrm{GO}-\mathrm{MoS_2/EO}$ implying that the former cools the boundary layer regime and heats the boundary (wall) whereas relatively speaking the latter heats the boundary layer and cools the wall (sheet).

5.2 ANN computation in MATLAB environment

To launch the neural network in the MATLAB environment, one has to execute the *nftool* command. This system features 4 inputs, 2 outputs and a 4-layer hidden structure, with 10 neurons in each hidden layer. For data division, 10% is designated for validation, 10% for testing, and the remaining 80% is allocated for training purposes. In this specific scenario, Bayesian regularization is applied as the training algorithm for more precise results, compared to other training options.

Table 6: Performance of the 10 runs of br-NN for $GO-MoS_2/Engine\ \ oil$:

Runs	MSE	Gradient	Mu	Num parameters	Sum squared s	Epochs
1	1.27162E-09	9.99E-08	50	32.1	863	404
2	1.19091E-09	1.00E-07	50	32.4	704	553
3	1.09196E-09	9.95E-08	500	36.5	928	403
4	1.30623E-09	9.86E-08	50	31.2	834	404
5	1.24283E-09	9.89E-08	50	32.7	1080	258
6	1.49953E-09	9.96E-08	500	35.6	844	525
7	1.22988E-09	9.89E-08	50	33.5	908	300
8	1.27294E-09	9.98E-08	50	33.0	915	447
9	1.08175E-09	9.93E-08	50	33.4	912	408
10	1.12010E-09	9.98E-08	50	33.4	942	297

Table 7: Performance of the 10 runs of br-NN for $Cu-SiO_2/Engine\ \ oil$:

Runs	MSE	Gradient	Mu	Num parameters	Sum squared parameters	Epochs
1	1.79687E-08	9.94E-08	500	32.8	935	678

2	1.13279E-09	9.98E-08	50	32.1	845	423
3	1.188617E-09	9.99E-09	500	32.9	900	624
4	2.20286E-09	9.94E-08	500	36.3	810	250
5	1.17278E-09	9.87E-08	50	32.7	934	335
6	1.35537E-09	9.91E-08	50	31.3	917	400
7	2.17436E-09	1.00E-09	500	36.9	883	410
8	1.57340E-09	9.97E-08	500	33.2	989	762
9	1.35404E-09	9.94E-08	50	34.7	942	350
10	1.35968E-09	9.91E-08	50	32.4	963	789

Tables 6 and 7 present the details of ten separate runs of the artificial neural network (ANN). The network was trained ten times for each scenario. The run with the lowest mean square error (MSE) was selected for discussion, as it exhibits the best performance among all other runs. The present article therefore focuses on the graph of training, performance, error histogram, fitting and regression for the run with the minimum MSE in each case.

6. RESULTS AND DISCUSSION

Computational estimates of different dimensionless parameters involved in present study have been presented in graphical/tabular forms. Using the numerical procedures described earlier Eqns. (7, 8) with boundary conditions (9) were solved numerically using the bvp4c package in MATLAB for several values of $Pr, R_d, A, M, s, Ec, \lambda, Br, Re_x, \epsilon, \varphi_1, \varphi_2$. Following this the ANN simulation was conducted via executing the *nftool* command. Data has been selected to represent physically viable hybrid magnetic nanofluid coating regimes and is summarized in **Table 8** with all relevant sources. Numerical results for various combinations of the thermal, magnetic and nanoscale (volume fraction) parameters are presented graphically in **Figures 3- 26.**

Table 8. Parametric values used in the present simulations

Parameters	Symbol	Value	Reference
Parameters of unsteadiness	A	$-0.5, 0.5, 1$	[69]
Suction/ injection parameter	s	-1, -0.5, 0, 0.5, 1	[70]
Radiation parameter	R_d	$0.2, 0.4, 0.6$	[69]
Volume fraction coefficient	φ_2	$0.01, 0.03, 0.05$	[70]

Prandtl number	Pr	$30, 40, 50$	[70]
Magnetic parameter	M	$1, 2, 3$	[69]
Inverse permeability parameter	ϵ	$0.5, 1, 1.5$	[69]
Eckert number	Ec	$0.001, 0.005, 0.01$	[69]
Thermal buoyancy	λ	$-0.5, 0, 0.5$	[70]
Reynolds number	Re_x	1	[71]
Brinkman Number	Br	$1, 2, 3$	[71]

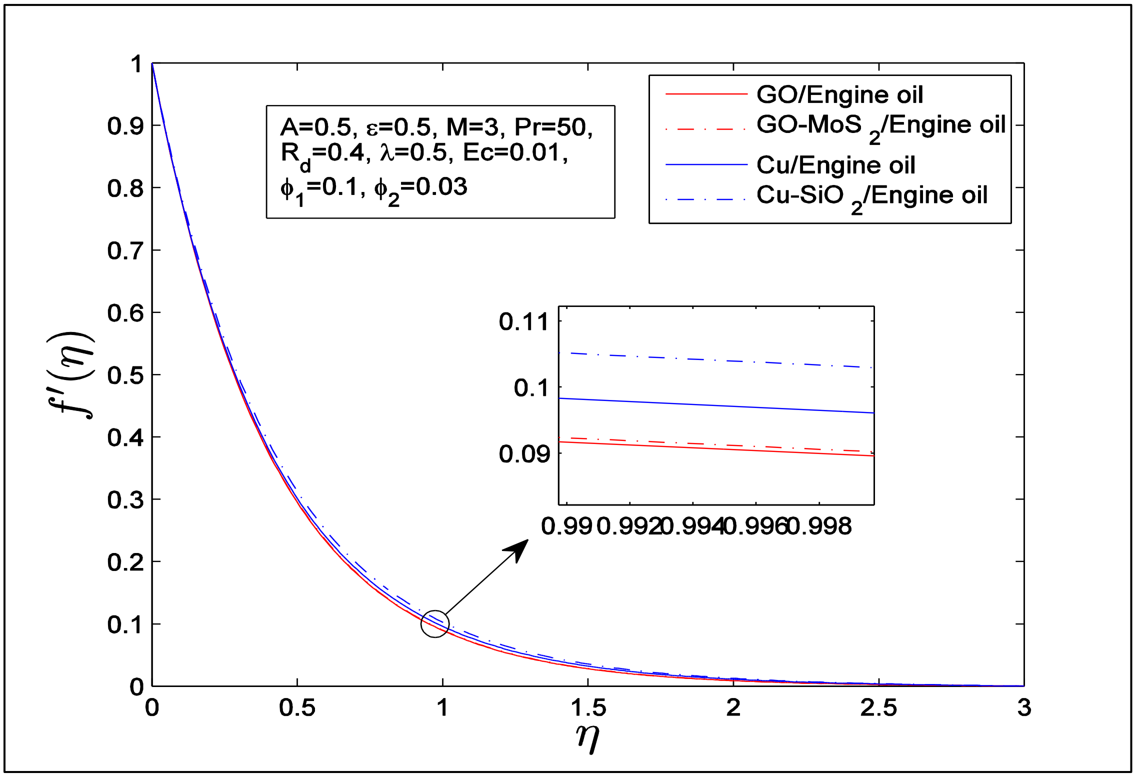

Figure 3: Velocity distribution for unitary and hybrid nanofluids

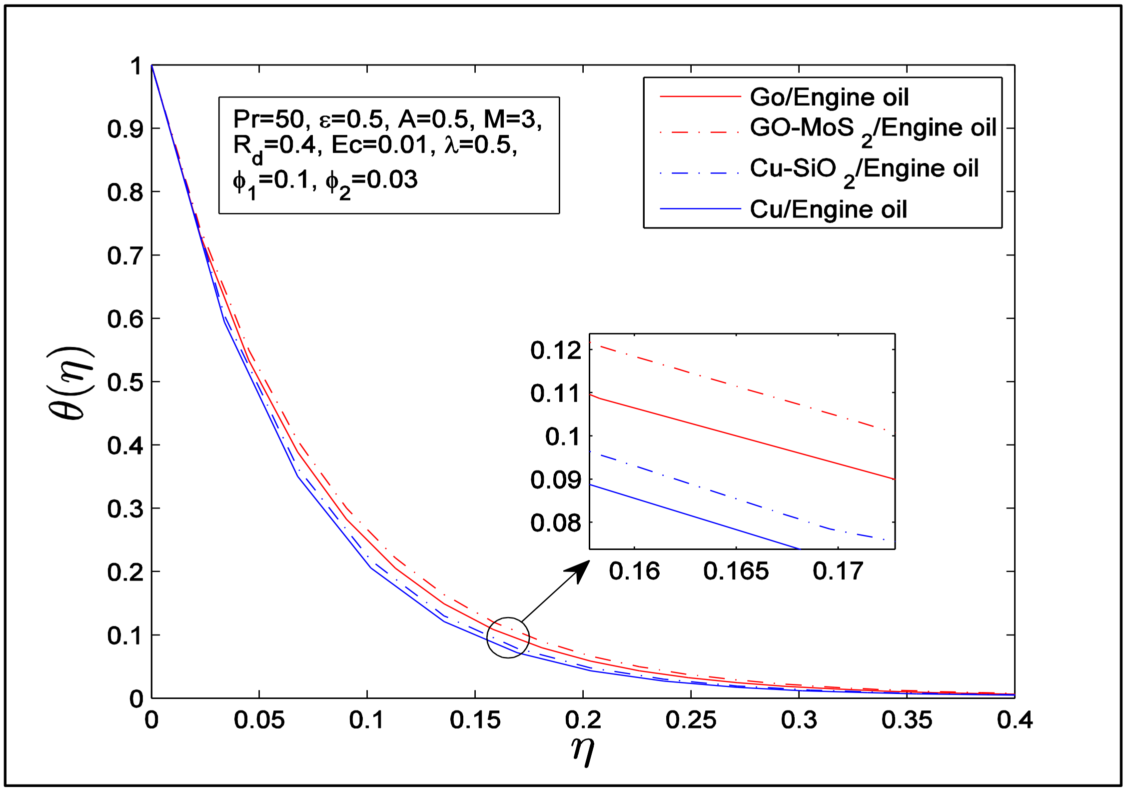

Figure 4: Temperature distribution for unitary and hybrid nanofluids

The profiles for velocity $f'(\eta)$ and temperature $\theta(\eta)$ for 2 unitary nanofluids ($\mathrm{GO/Engine\ oil}$ and $\mathrm{Cu/Engine\ oil}$) and 2 hybrid nanofluids ($\mathrm{GO-MoS_2/Engine\ oil}$ and $\mathrm{Cu-SiO_2/Engine\ oil}$) on are displayed in figures (3) and (4). Fig. 3 shows that with a second nanoparticle present i. e. ϕ_2>0, for the hybrid nanofluids, there is an elevation in velocity relative to unitary nanofluids ($\phi_2 = 0$). The boundary layer flow is accelerated therefore, and momentum boundary layer thickness will be reduced. The $\mathrm{Cu-SiO_2/Engine\ oil}$ hybrid nanofluid clearly achieves higher velocity magnitudes compared with the $\mathrm{GO-MoS_2/Engine\ oil}$, indicating that viscosity is reduced in the former which produces greater flow acceleration. In all profiles there is a smooth asymptotic convergence achieved in the free stream confirming that sufficiently large infinity boundary condition has been prescribed in the MATLAB bvp4c computations. Fig. 4 indicates that for all 4 nanofluids studied there is a smooth descent in temperatures from the wall to the free stream. $\mathrm{GO/Engine\ oil}$ supersedes $\mathrm{Cu/Engine\ oil}$ temperatures at all locations in the boundary layer. Thermal boundary layer thickness is also greater for the former. However significantly higher temperature is computed with the $\mathrm{GO-MoS_2/Engine\ oil}$ hybrid nanofluid compared with both unitary nanofluids. The $Cu - SiO_2/\mathrm{Engine}$ oil hybrid nanofluid temperature exceeds that of the Cu/Engine oil unitary nanofluid but is not as high as the GO/Engine oil unitary nanofluid. Clearly the unique nanoparticle contributions exert a different overall impact on thermal conductivity of the nanofluid. Effectively graphene oxide combined with molybdenum sulphide ($GO - MoS_2/\mathrm{Engine}$ oil hybrid nanofluid) is observed to achieve the best thermal enhancement properties which is contrary to its performance in the velocity distribution (Fig.3). The amalgamation of *carbon-based and metallic nanoparticles* would therefore appear to be more efficient than purely metallic or carbon-based nanoparticles. Nevertheless, no single nanofluid whether unitary or hybrid simultaneously attains the best velocity or thermal performance.

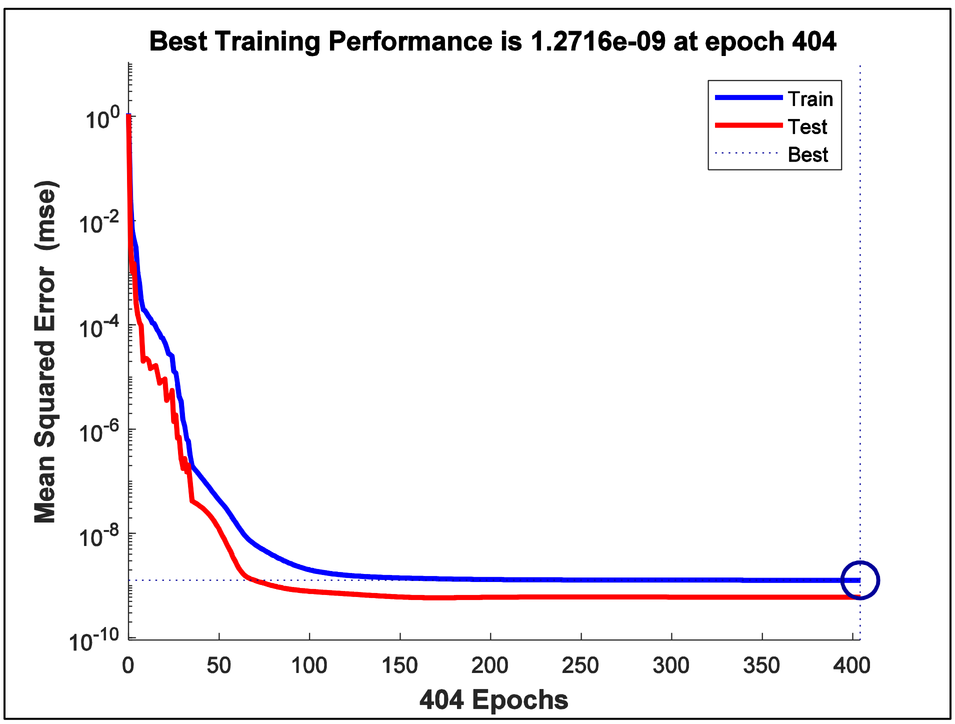

(a) Mean square error

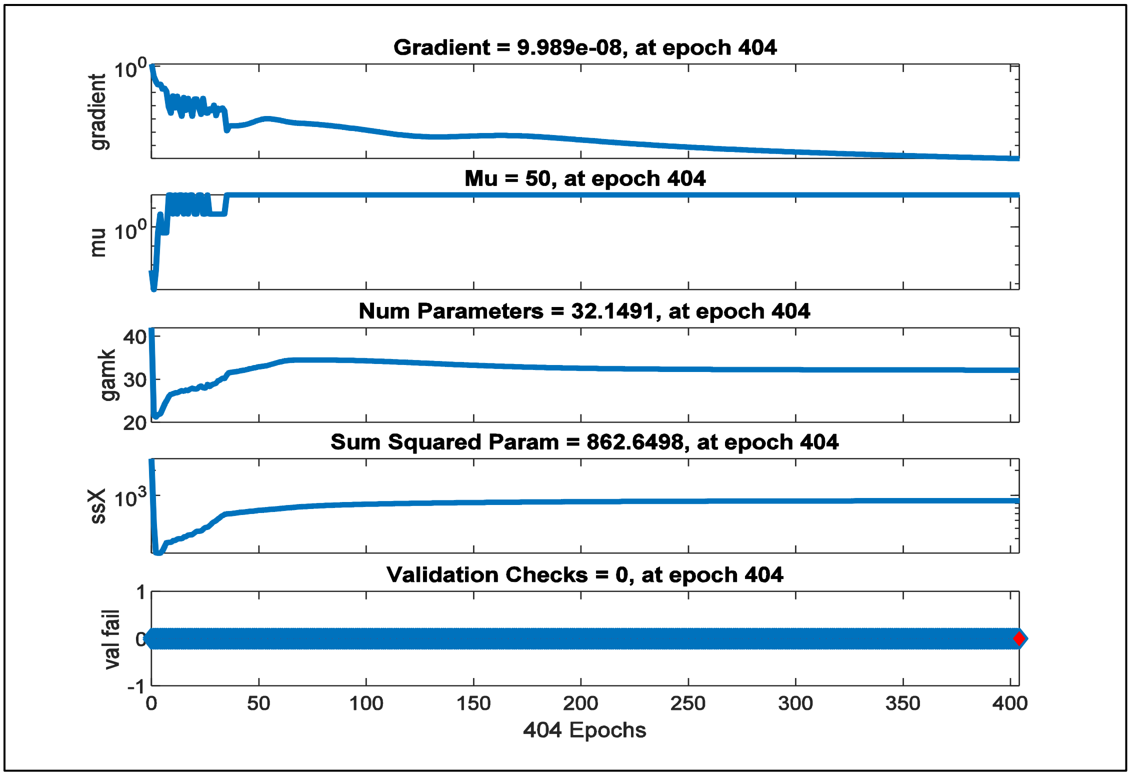

(b) Gradient of MU

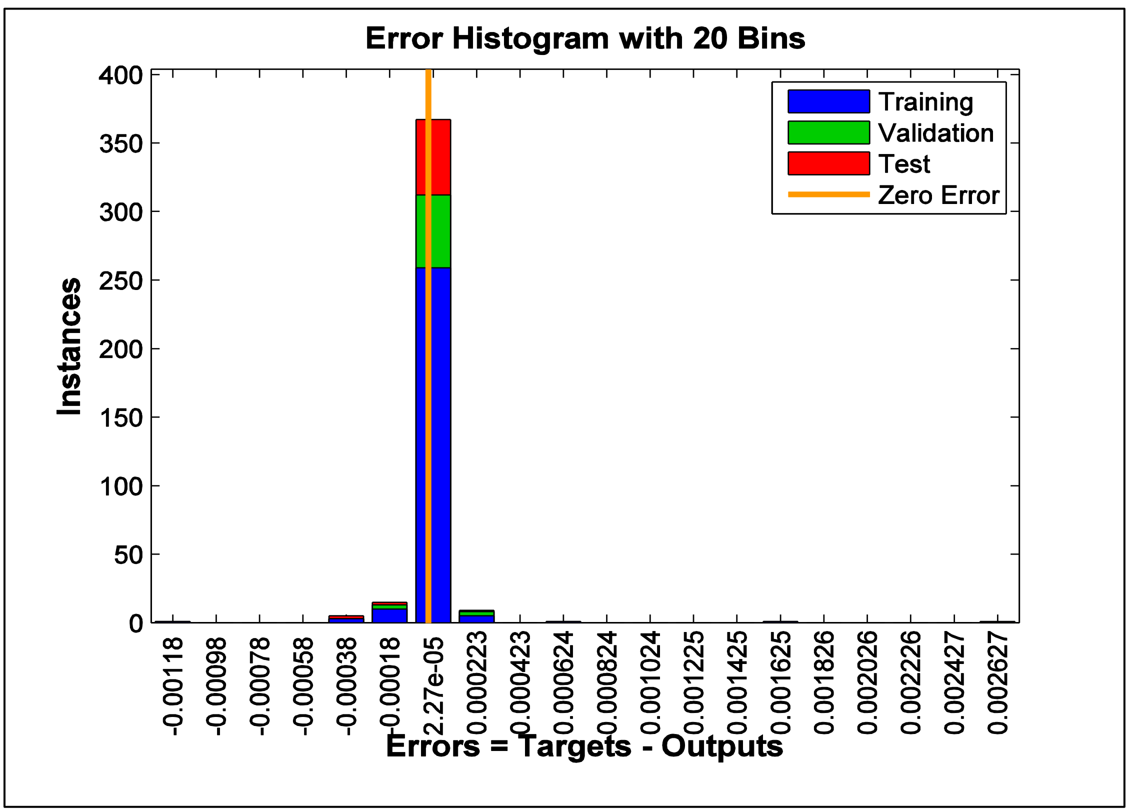

(c) Error Histogram

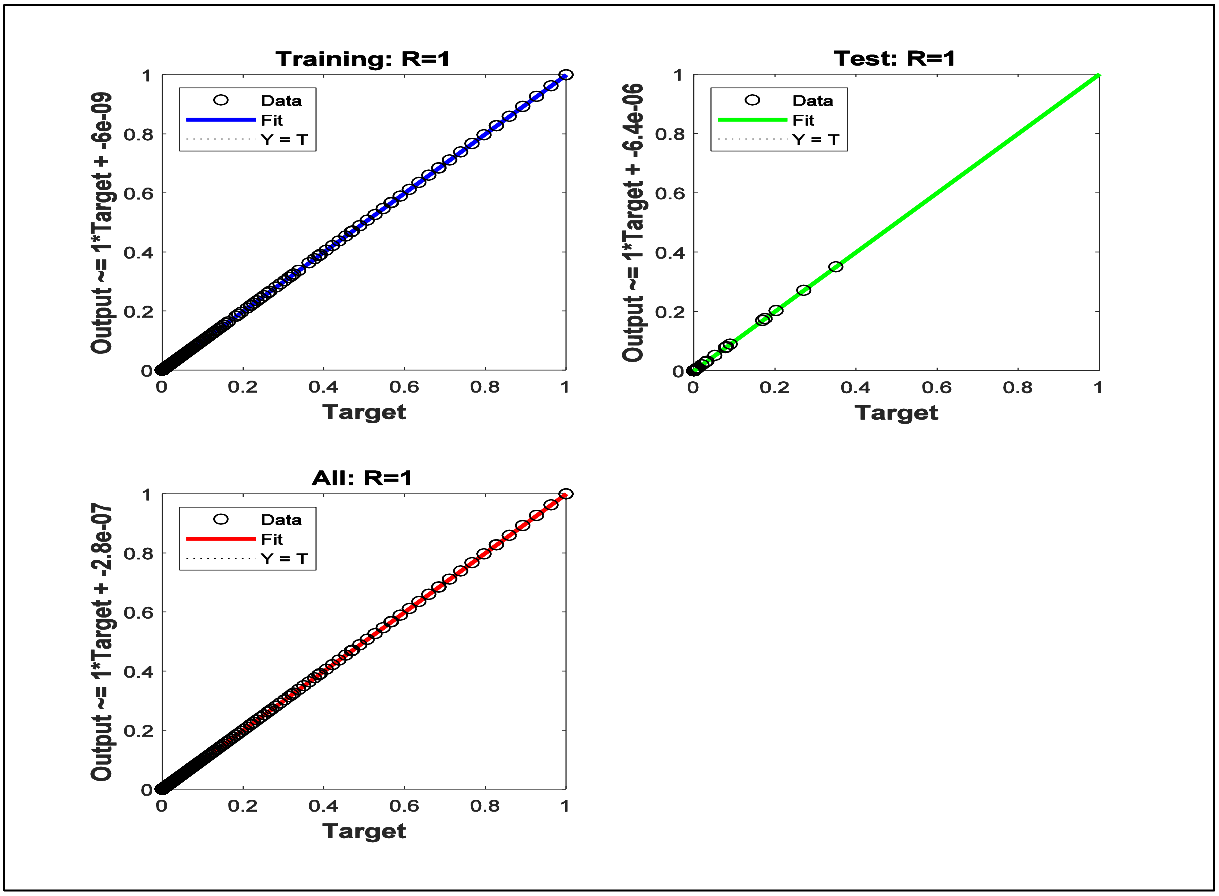

(d) Regression

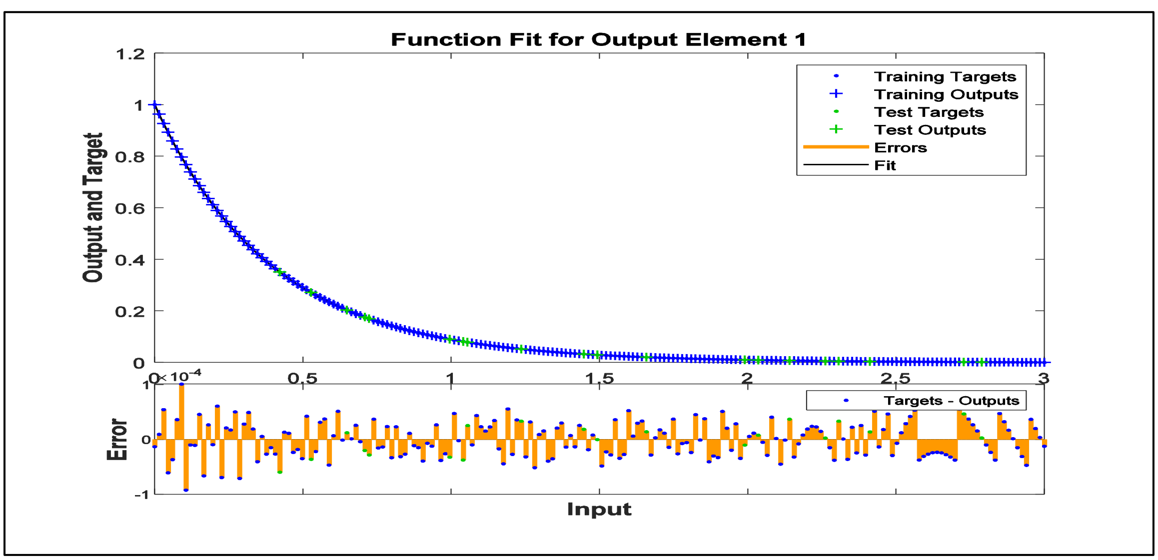

(e) Fitting

Figure 5: Mean square error, gradient, MU, regressions and fitting for $GO - MoS_2$/Engine oil

The $\mathrm{GO-MoS_2/Engine\ oil}$ hybrid nanofluid case has first been analyzed using neural networks incorporating Bayesian regularization as the training algorithm. In sub-figure 5(a), the mean square error was found to be attain a minimum value at 404 epochs, displaying a small error of almost 10^{-8}. The training graphs in sub-figure 5(b) visualize all key outputs, namely gradient, Mu, number of parameters and sum of squared parameters values of $9.99 \times 10^{-8}, 50, 32.1$ and 863 respectively. The error histogram in sub-figure 5(c) shows that the errors approach the zero-error line of approximately 2.7×10^{-5}. Sub-figure 5(d) illustrates the regression plots, which present a correlation assessment of R close to unity, a highly desirable outcome for testing, validation and training. Finally, sub-figure 5(e) displays the fitness graph, displaying the maximum error during testing, validation, and training being less than 1×10^{-4}

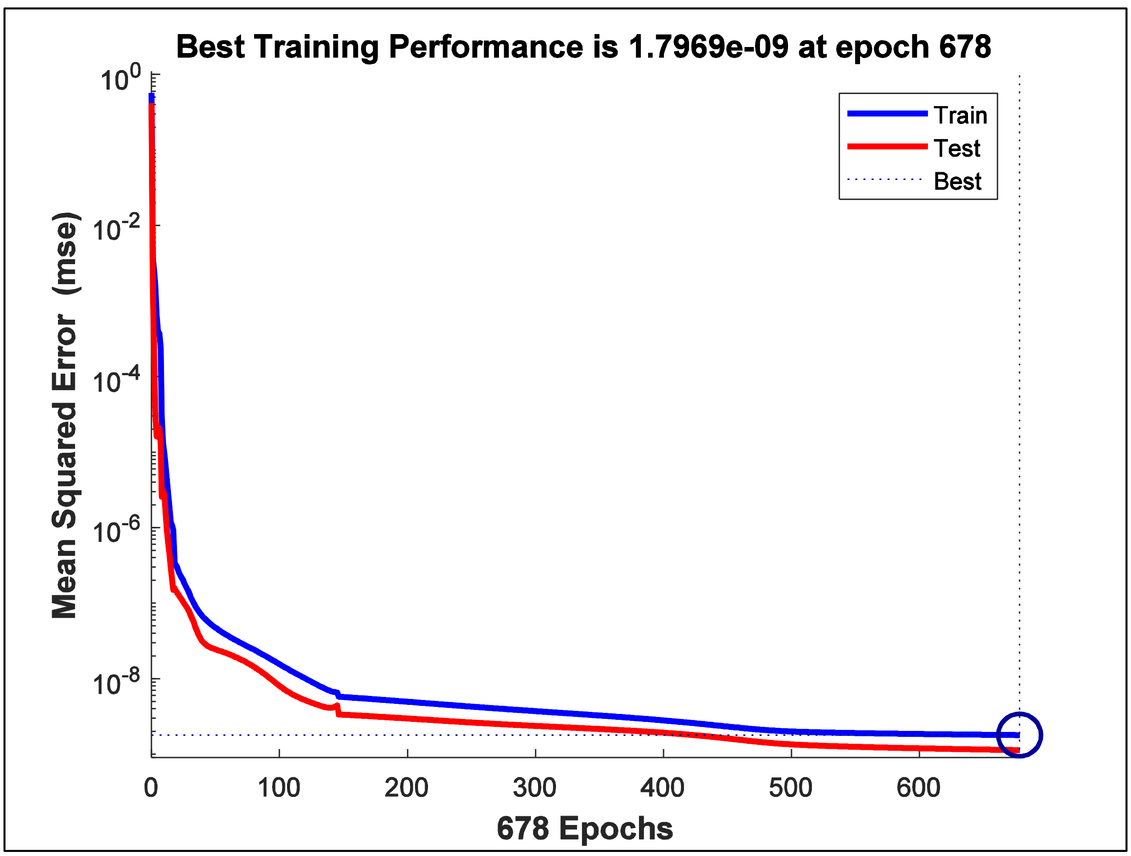

(a) Mean Squared Error

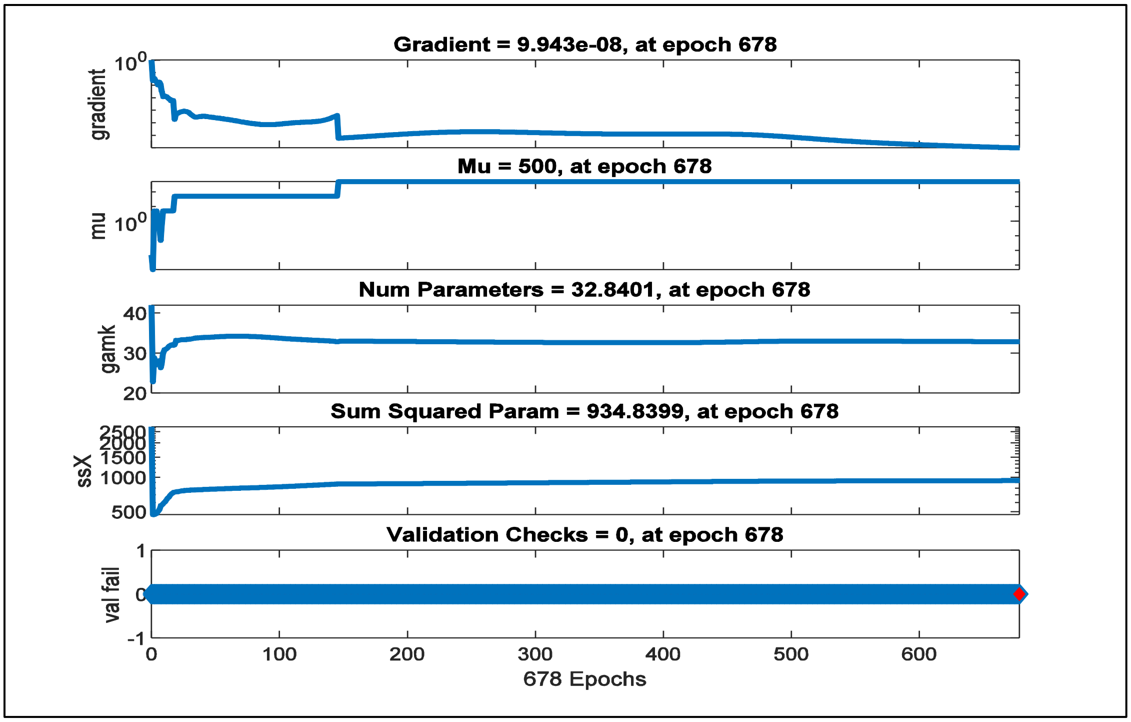

(b) Gradient and MU

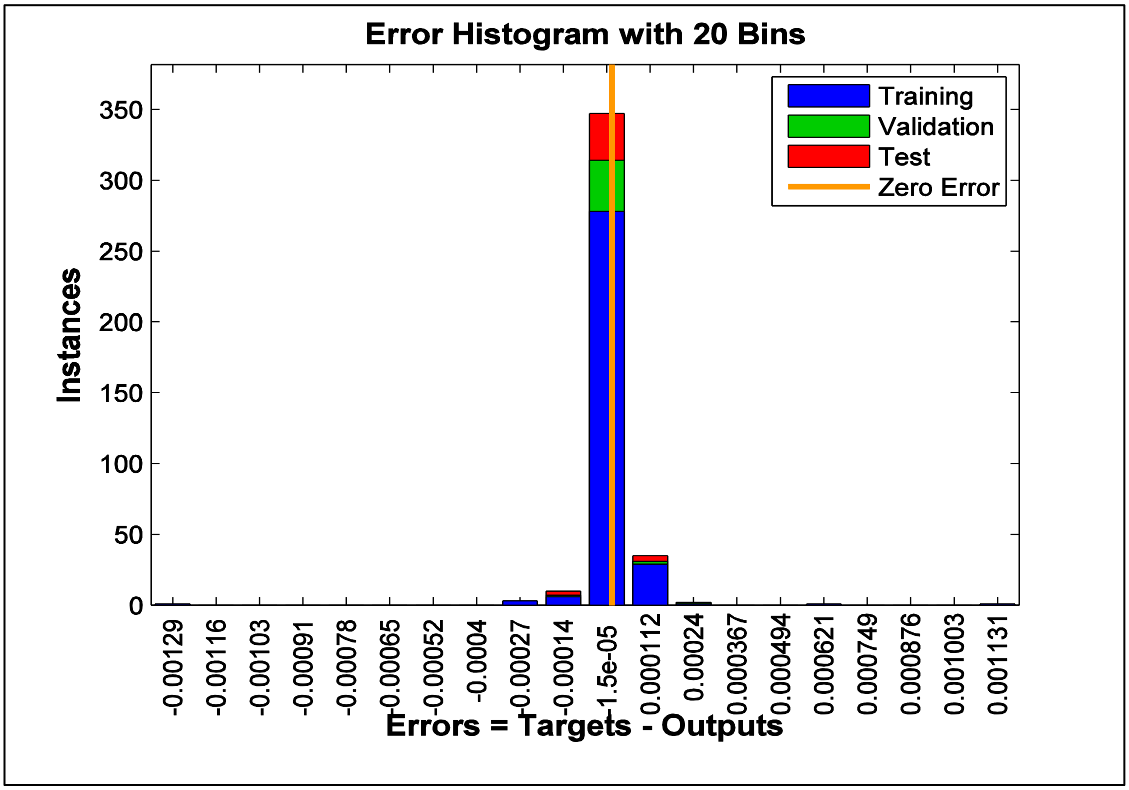

(c) Error Histogram

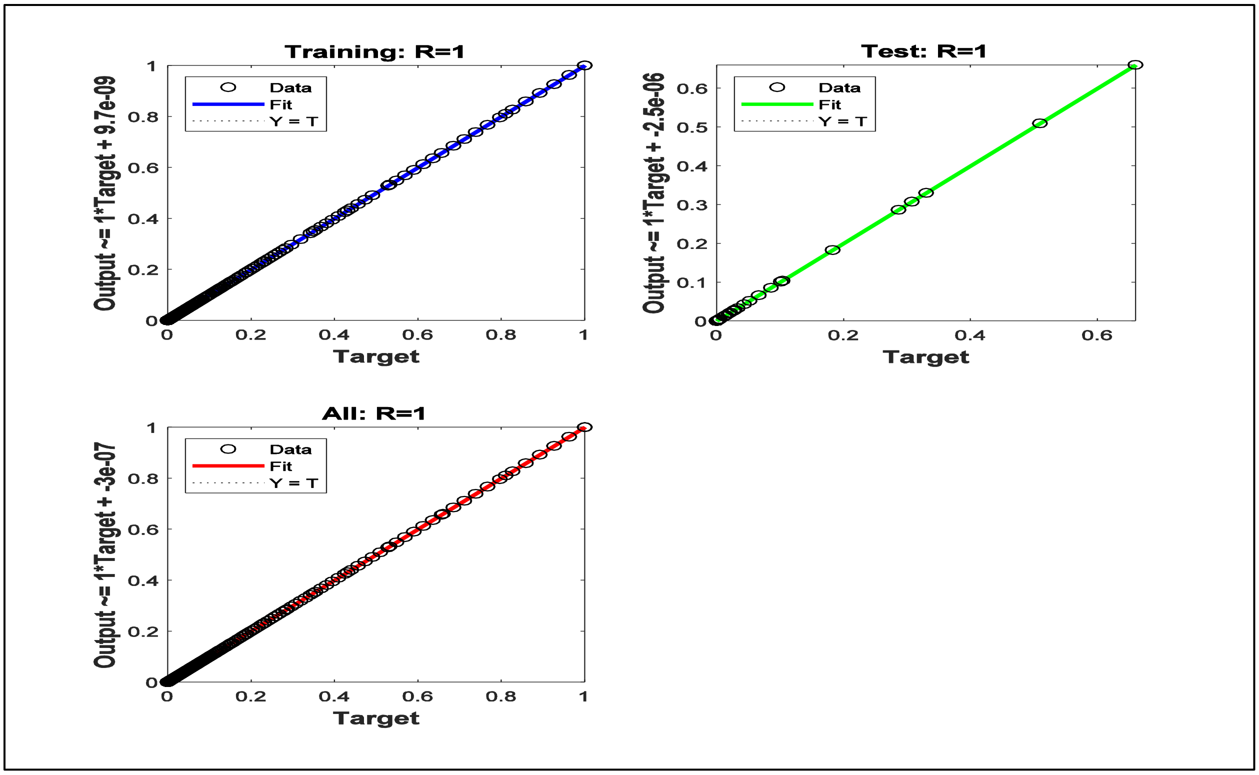

(d) Regressions

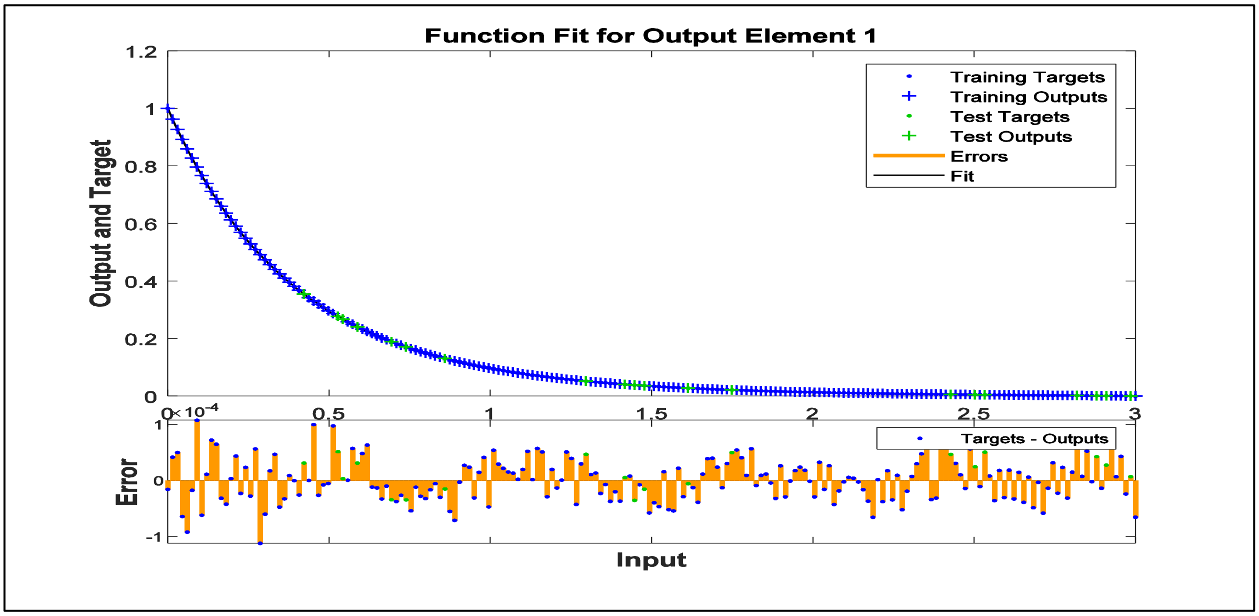

(e) Fitting

Figure 6: Mean square error, gradient, MU, regressions and fitting for $Cu - SiO_2$/Engine oil

Next the $Cu-SiO_2$/Engine oil hybrid nanofluid case has been studied again using neural networks incorporating Bayesian regularization as the training algorithm. In sub-figure 6(a), the mean square error is now observed to attain its minimum at 678 epochs (a much higher value than the 404 epochs computed in the $GO-MoS_2$/Engine oil hybrid nanofluid case, Fig 5a)), displaying a small error of almost 10^{-8}. The training graphs in sub-figure 6(b) again visualize gradient, Mu, number of parameters, and sum of squared parameters values of $9.99 \times 10^{-8}, 500, 32.8$ and 935, respectively, The error histogram in sub-figure 6(c) shows the errors approach a zero error line of approximately -1.5×10^{-5} which in this case is sub-zero, whereas in the $GO-MoS_2$/Engine oil hybrid nanofluid case (Fig 5c) the value is positive i.e. approximately 2.7×10^{-5}. Sub-figure 6(d) illustrates the regression plots, which again present a correlation assessment of R close to unity, indicating that again a beneficial outcome is achieved as with the $GO-MoS_2$/Engine oil hybrid nanofluid case (Fig 5d) for testing, validation, and training. Finally, sub-figure 6(e) displays the fitness graph, displaying the maximum error during testing, validation and training is again less than 1×10^{-4} which concurs with the $GO-MoS_2$/Engine oil hybrid nanofluid case (Fig. 5e).

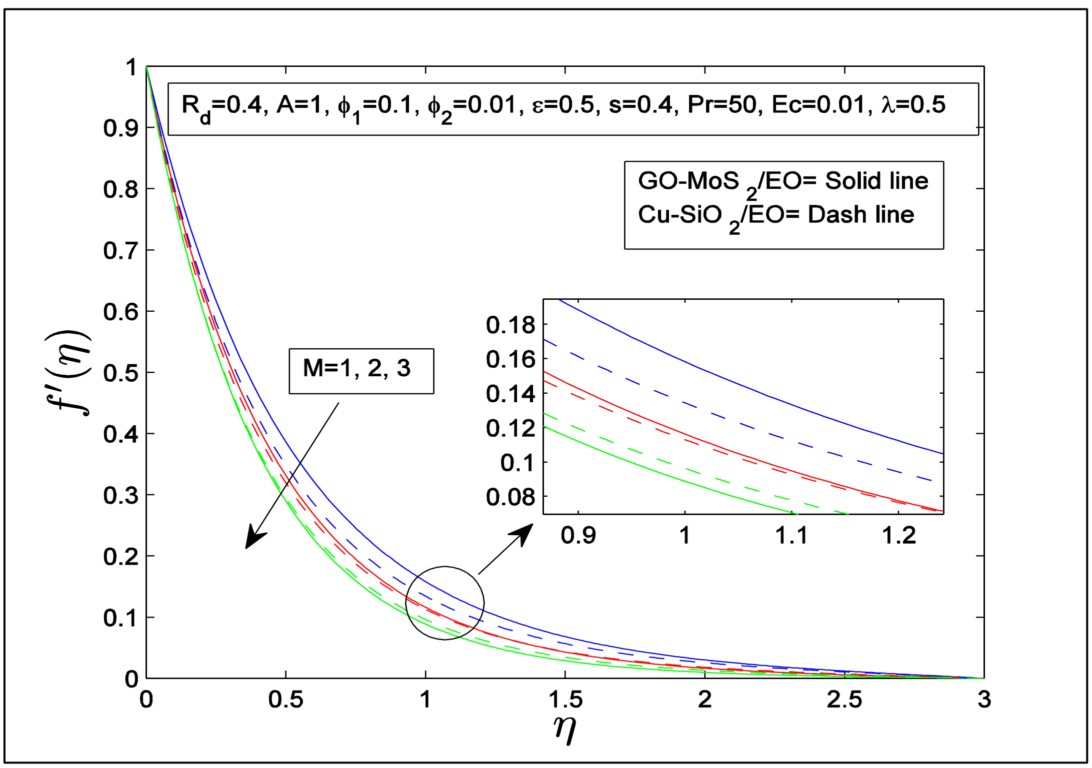

Figure 7. Velocity distribution for various values of M

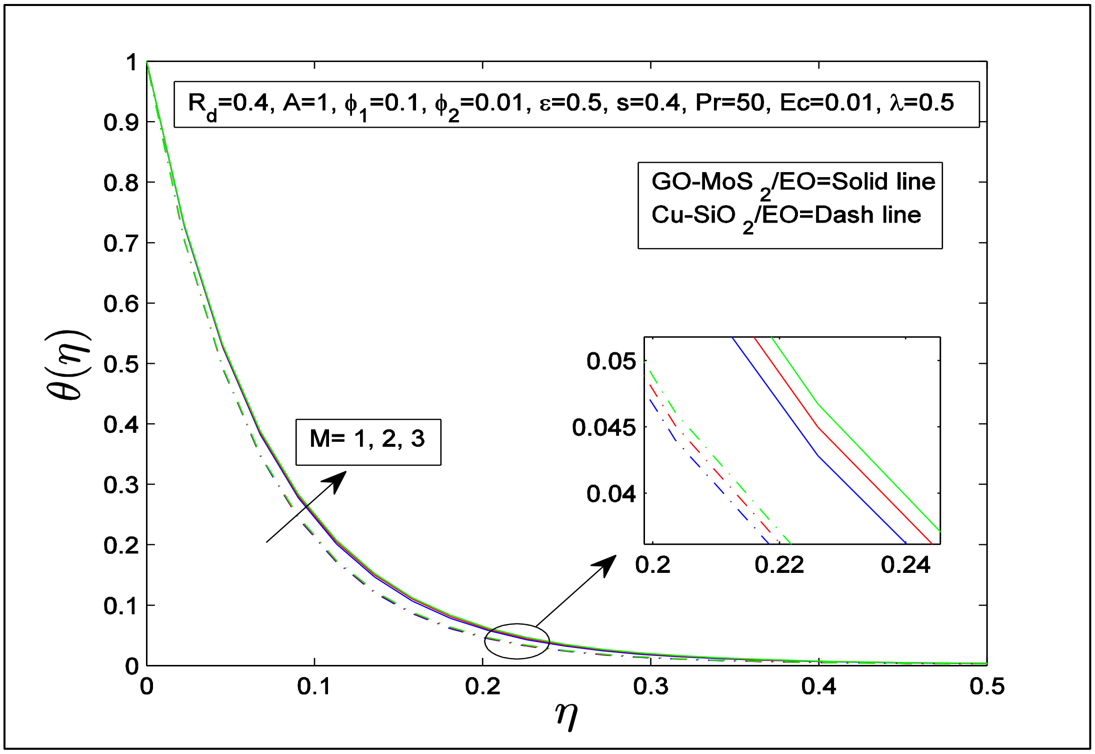

Figure 8. Temperature distribution for various values of *M*

In figures (7) and (8), the influence of increasing magnetic parameter M, on the velocity and temperature distributions is visualized. Fig. 7 shows that the velocity $f'(\eta)$ is damped significantly for all unitary and hybrid nanofluids with increment in magnetic parameter. Hydrodynamic (momentum) boundary layer thickness is therefore elevated. The presence of the Lorentz magnetic body force, $-\frac{\sigma_{hnf}/\sigma_f}{\rho_{hnf}/\rho_f} M f'(\eta)$ featured in Eqn. (8), creates a strong damping effect which decelerates the blood flow and increases momentum boundary layer thickness. The parameter *M* is sometimes known as Stuart number and embodies the relative contribution of Lorentzian magnetic drag to inertial force. It is therefore distinct from the more familiar Hartmann number which represents the ratio of Lorentz magnetic force to viscous force in the regime. For $M = 1$ both inertial and magnetic Lorentz forces contribute equally. For $M > 1$ the Lorentz force dominates the inertial force. At all values of *M*, the $\mathrm{GO-MoS_2/Engine}$ oil achieves distinctly greater velocity magnitudes than the $\mathrm{Cu-SiO_2/Engine}$ oil. This may be related to both the weaker magnetic response of the former to external magnetic field and/or the lower global viscosity of this hybrid nanofluid. Both these factors will reduce the impact of Lorentzian body force and will produce a thinner momentum boundary layer thickness. The disparity between the velocity profiles for the two hybrid nanofluids is also found to be reduced at stronger magnetic field i. e. the profiles are more clustered when *M = 3 compared with when M = 1*.

Fig. 8 visualizes the temperature $\theta(\eta)$ response with increment in M and a weak elevation in temperatures is computed for both hybrid nanofluids. The hybrid nanofluids have to perform supplementary work in dragging against the action of the magnetic field. As magnetic field is increased this additional energy expenditure is elevated. This work is dissipated as thermal energy in the nanofluid which manifests naturally in an escalation in temperature. Thermal boundary layer thickness is therefore also increased. Consistently the $\mathrm{GO-MoS_2/Engine\ oil}$ case exhibits higher temperatures (and greater thermal boundary layer thickness) than $\mathrm{Cu-SiO_2/Engine\ oil}$ case. Additionally, the profiles are all separate for each nanofluid and not clustered as with the velocity profiles (Fig. 7). Although there is no direct contribution of magnetic field in the energy eqn. (8)., it is strongly coupled to the momentum eqn. (7) via multiple terms including the convective terms, $-f'(\eta)\theta(\eta)+f(\eta)\theta'(\eta)$ and the viscous heating term, $+\frac{\mu_{hnf}/\mu_f}{(\rho C_p)_{hnf}/(\rho C_p)_f}Ec\{f''(\eta)\}^2$. Mathematically the influence of magnetic field is therefore experienced indirectly by the temperature distribution, although the effect is less pronounced understandably than in the velocity distribution since the latter is affected directly by the Lorentzian linear magnetic body force.

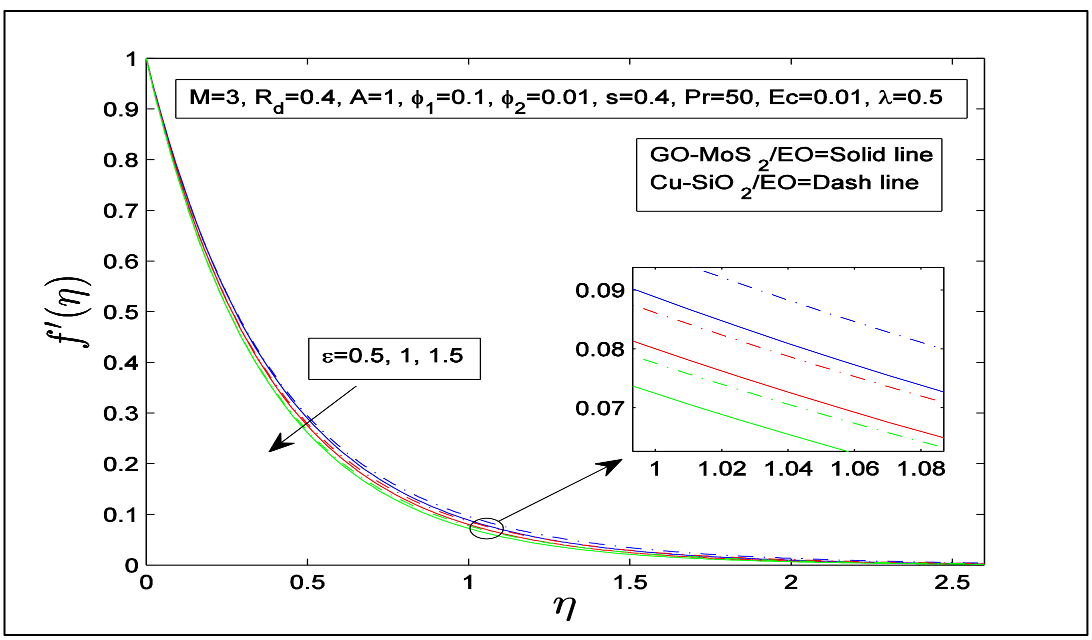

Figure 9. Velocity distribution for various values of ϵ

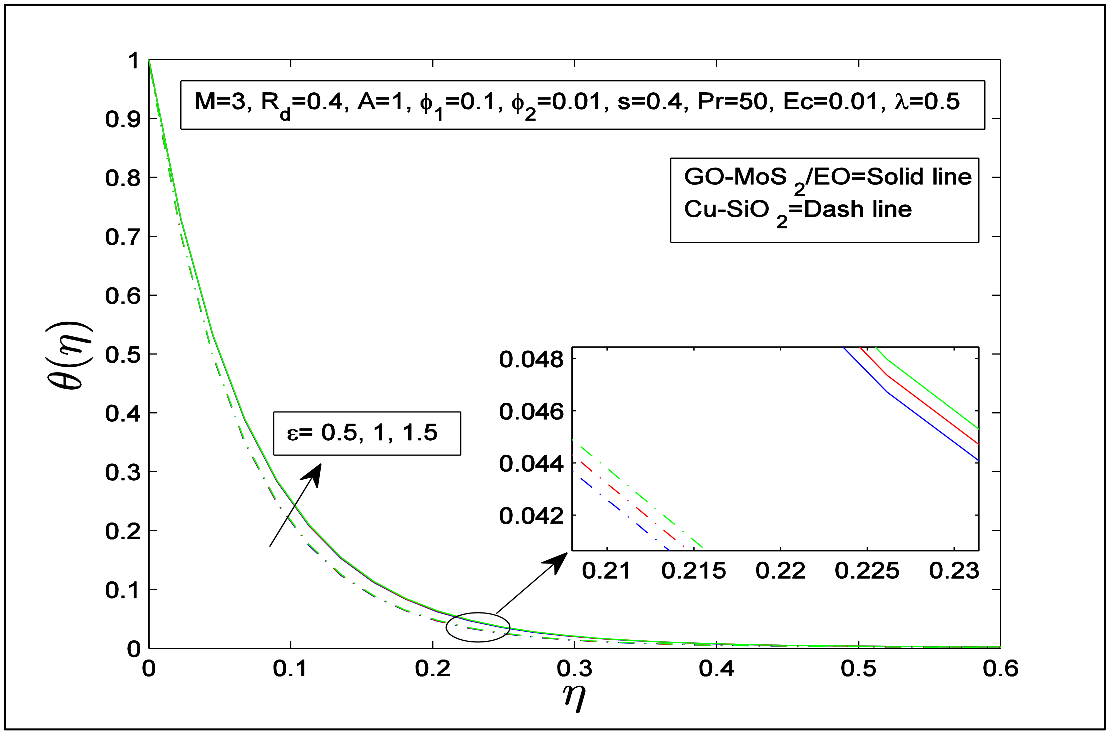

Figure 10. Temperature distribution for various values of ϵ

In figures (9) and (10), the responses of velocity and temperature to variation in inverse permeability parameter, ϵ, have been plotted. Fig. 9 shows that velocity magnitude $f'(\eta)$ is reduced at all values of transverse coordinate (η) with increment in ϵ. $\epsilon = \frac{\vartheta_f(1-ct)}{aK}$ and is clearly inversely proportional to the porous medium permeability, K. It features in the Darcian linear bulk matrix impedance force in the momentum eqn. (7), viz $\frac{\vartheta_{hnf}}{\vartheta_f}\{-\epsilon f'(\eta)\}$. As K is decreased therefore ϵ is increased and the Darcian drag effect is amplified. This decelerates the boundary layer flow for both hybrid nanofluids, although the velocities computed for $\mathrm{Cu-SiO_2/Engine\ oil}$ exceed those observed for $\mathrm{GO-MoS_2/Engine\ oil}$. The decrease in permeability implies an elevation in the concentration of solid fibers in the porous medium which inhibits percolation. This decelerates the flow and increases momentum boundary layer thickness although the latter is of lower magnitude for $\mathrm{Cu-SiO_2/Engine\ oil}$ hybrid nanofluid (since velocity magnitudes are higher). The resistive effect of lower permeability offers an excellent mechanism for flow regulation. However, it does not induce flow reversal or separation (back flow) since at all locations in the boundary layer only positive values of velocity are computed. Fig. 10 reveals that increment in inverse permeability parameter, ϵ, there is a marked boost in temperatures computed again for both hybrid nanofluids. The decrease in permeability as explained earlier corresponds to a hike in volume of solid fibers present. This encourages thermal conduction and produces a heating effect in the regime, as noted by Tien and Vafai [75]. Thermal boundary layer thickness will therefore also be accentuated with increasing inverse permeability parameter, ϵ. With larger value of ϵ, $GO - MoS_2$/Engine oil produces higher temperatures and greater thermal boundary layer thickness than $Cu - SiO_2$/Engine oil (the converse response to that computed for the velocity field, Fig. 9).

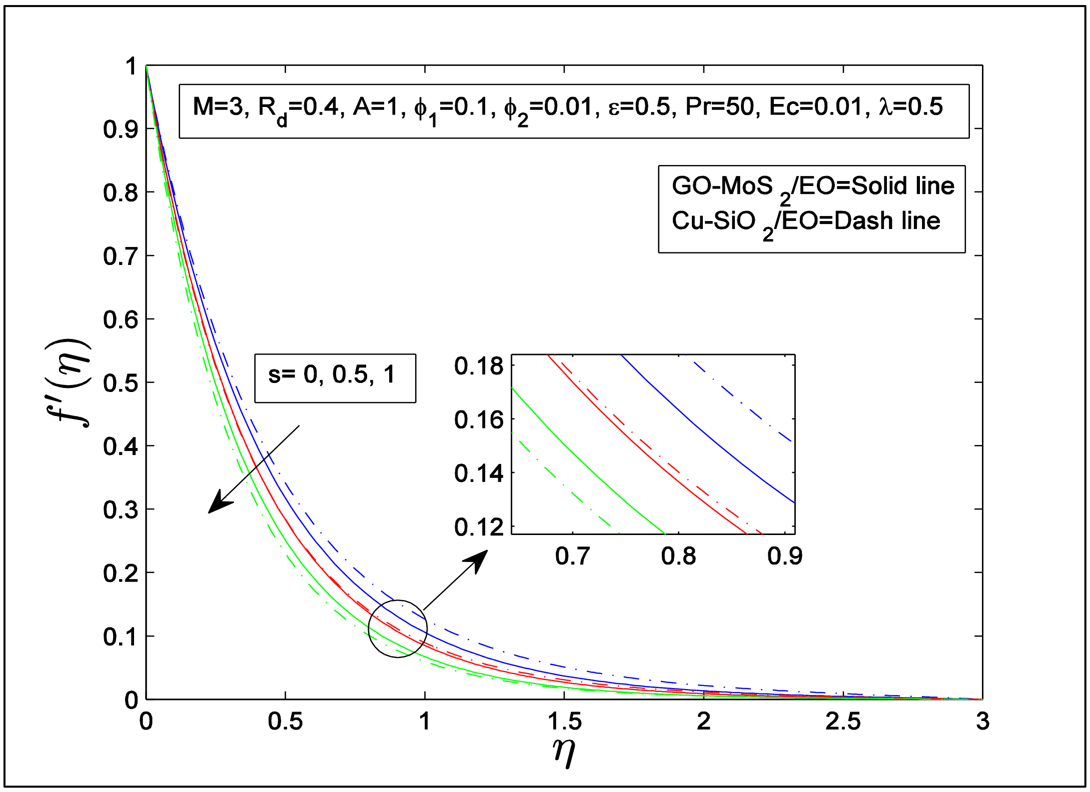

Figure 11. Velocity distribution for various values of s.

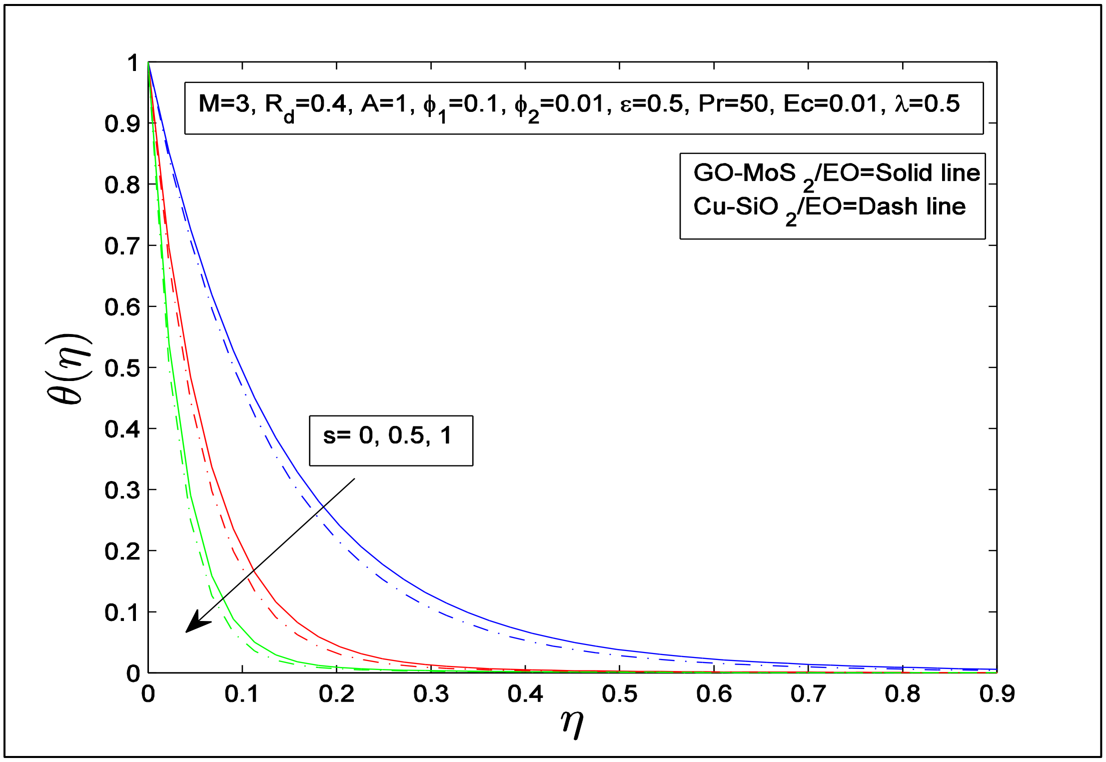

Figure 12. Temperature distribution for various values of *s*

In figures (11) and (12), we observe that with increasing suction parameter ($s > 0$), the velocity $f'(\eta)$ and the temperature magnitude $\theta(\eta)$ are decreased. Stronger suction at the porous wall (sheet) withdraws hybrid nanofluid out of the boundary layer and destroys momentum. This induces greater adherence of the nanofluid to the wall and decelerates the flow (Fig. 11) resulting in a thicker momentum boundary layer. Via coupling of the momentum eqn. (7) with the energy eqn. (8) due to natural convection, the temperature (Fig. 12) is also depleted in the regime. Thermal boundary layer thickness will therefore be reduced with stronger suction. For the velocity distribution (Fig. 11) $\mathrm{Cu-SiO_2}$/Engine oil attains higher velocities whereas for the temperature distribution, $\mathrm{GO-MoS_2}$/Engine oil shows higher magnitudes. The case of $s = 0$ corresponds to a solid wall (non-perforated sheet) and as anticipated produces maximum velocity and maximum temperature for both hybrid nanofluids. Clearly successful thermal management may be achieved with strong wall suction in addition to flow control, both of which are of considerable interest in nano-coating operations as emphasized by Koch [76].

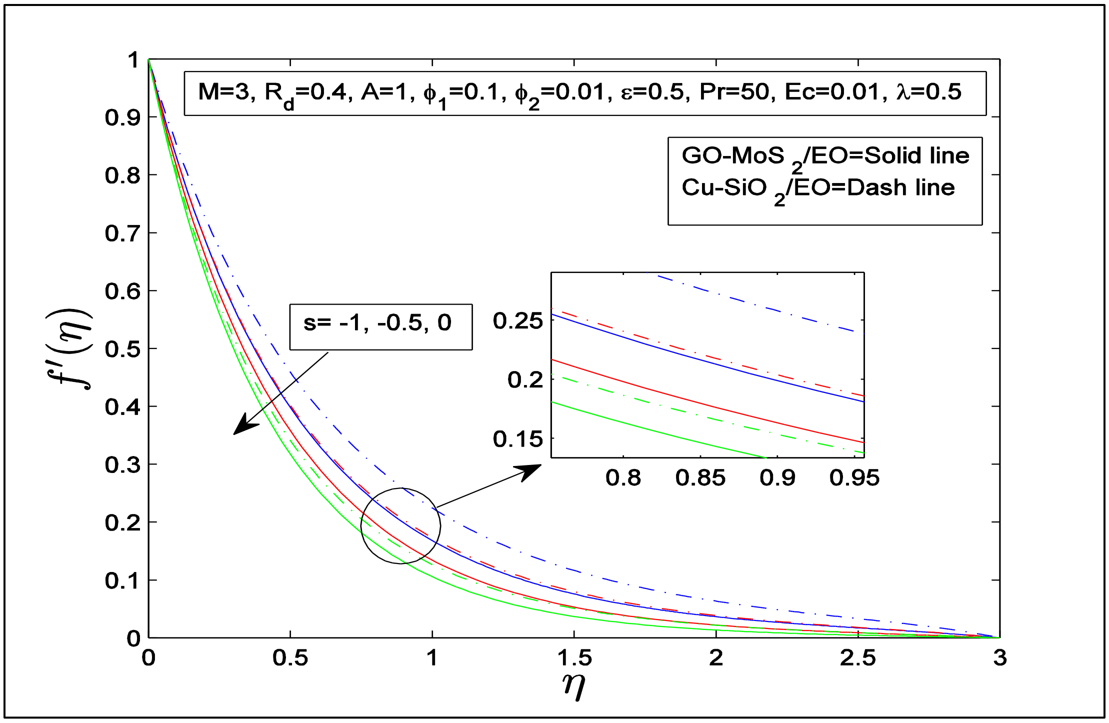

Figure 13. Velocity distribution for various values of *s*

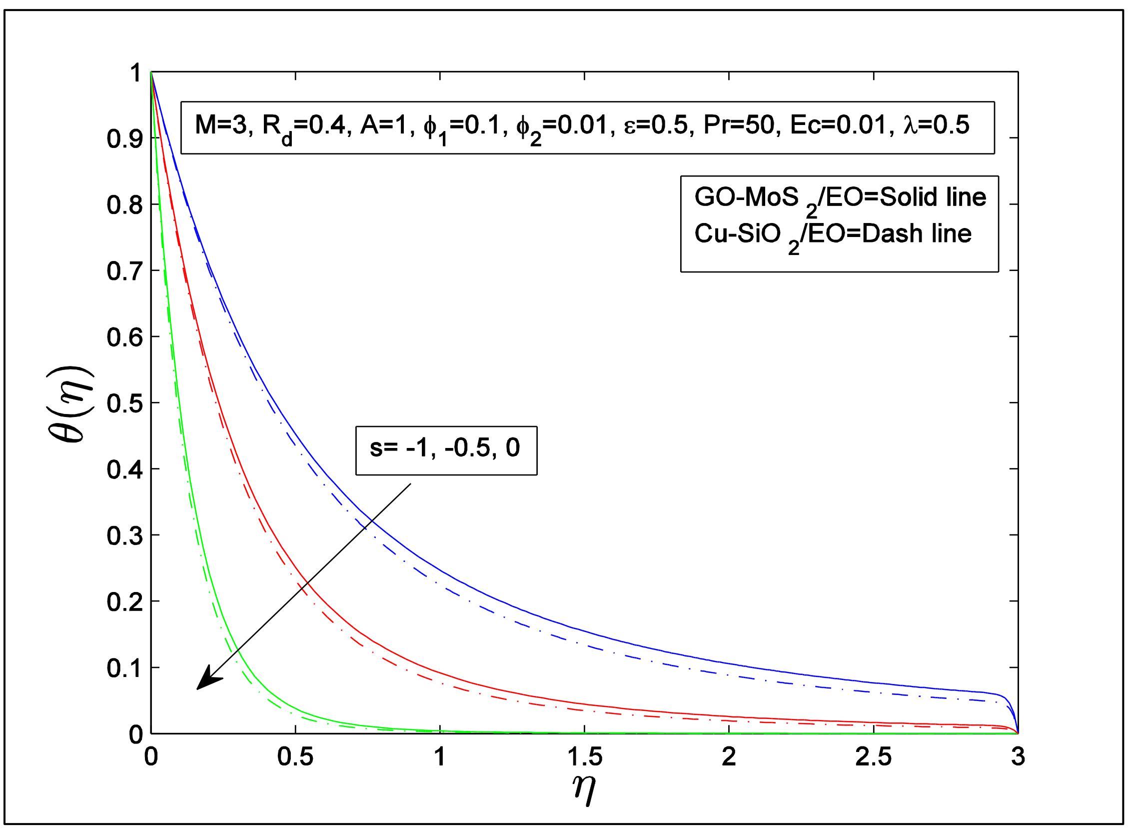

Figure 14. Temperature distribution for various values of *s*

In figures (13) and (14), the influence of increasing injection parameter ($s < 0$) on velocity profiles $f'(\eta)$ and the temperature profile $\theta(\eta)$ is presented. The opposite trends are computed as observed for suction (Figures 11, 12). With increasing injection strong flow acceleration is induced due to the addition of more hybrid nanofluid through pores of the stretching wall. This aids momentum development and decreases hydrodynamic boundary layer thickness (Fig. 13). Slightly greater velocity values are computed for $\mathrm{Cu} - \mathrm{SiO_2}/\mathrm{Engine\ oil}$, as also observed in the suction case (Fig. 11). Temperature (Fig. 14) is similarly enhanced with increment in injection (blowing) leading to larger thermal boundary layer thickness. Again, as in the case for suction, the $\mathrm{GO} - \mathrm{MoS_2}/\mathrm{Engine\ oil}$ hybrid nanofluid attains superior temperature values. For the solid wall case (*s* = *0*), minimal velocity and temperature are computed at all positions in the boundary layer.

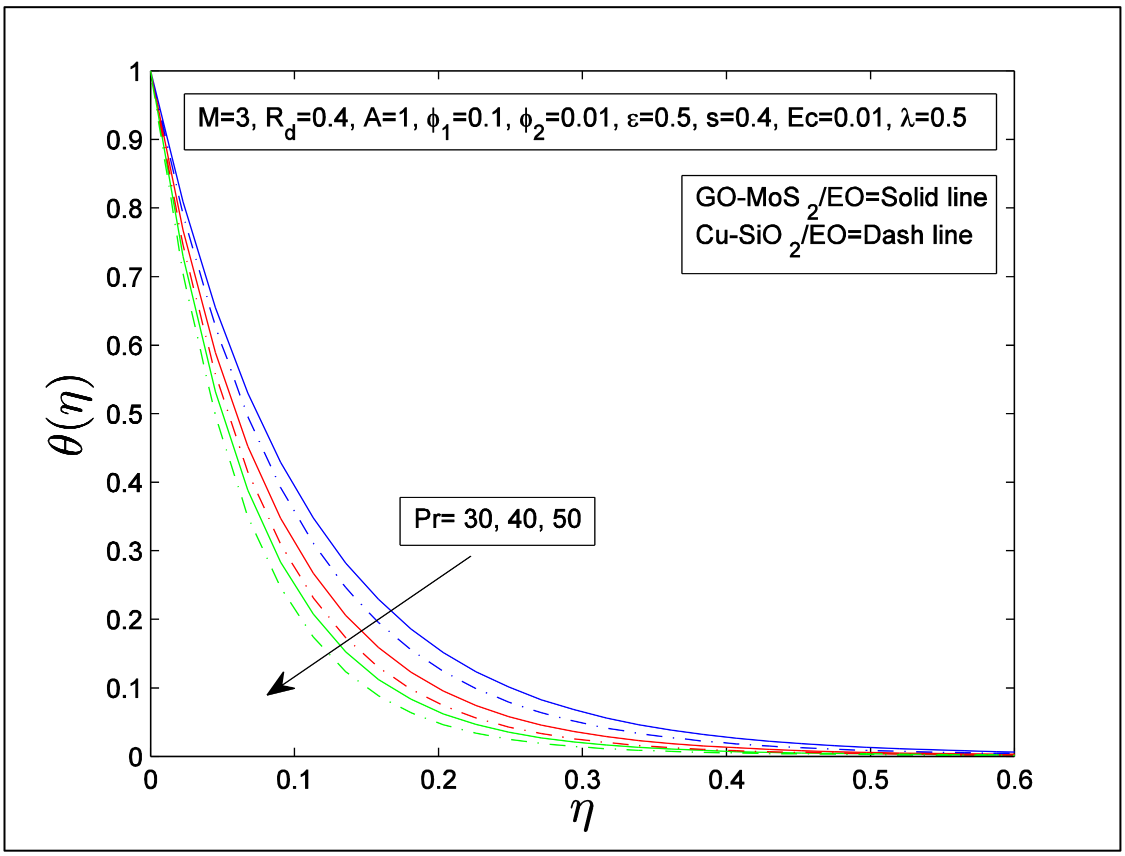

Figure 15. Temperature distribution for various values of Pr

Figure (15) depicts the evolution in temperature, $\theta(\eta)$ with increasing Prandtl number Pr. A strong decrement is computed. It is noteworthy that large Prandtl numbers are assigned to physically represent actual hybrid nanofluids utilizing a base fluid of engine oil. The Prandtl number is inversely related to thermal conductivity. Oil-based nanofluids therefore have very high Prandtl numbers since the base fluid thermal conductivity is generally low. One objective of doping the nano-coatings with combinations of metallic (e. g. copper, molybdenum) and carbon-based nanoparticles (e. g. graphene) is to enhance the thermal conductivity of the nano-coatings. For *Pr* >> 1 thermal diffusivity is greatly exceeded by momentum diffusivity in the nanofluid. This inhibits thermal transport and cools the boundary layer resulting in a depletion in temperature and also thermal boundary layer thickness. The $\mathrm{GO-MoS_2}$/Engine oil hybrid nanofluid again clearly achieves higher temperatures relative $\mathrm{Cu-SiO_2}$/Engine oil hybrid nanofluid and will produce a greater thermal boundary layer thickness. The temperature distribution will also influence the heat transmission to the wall. Therefore, a more prominent cooling of the wall can be achieved with the deployment of $\mathrm{GO-MoS_2}$/Engine oil.

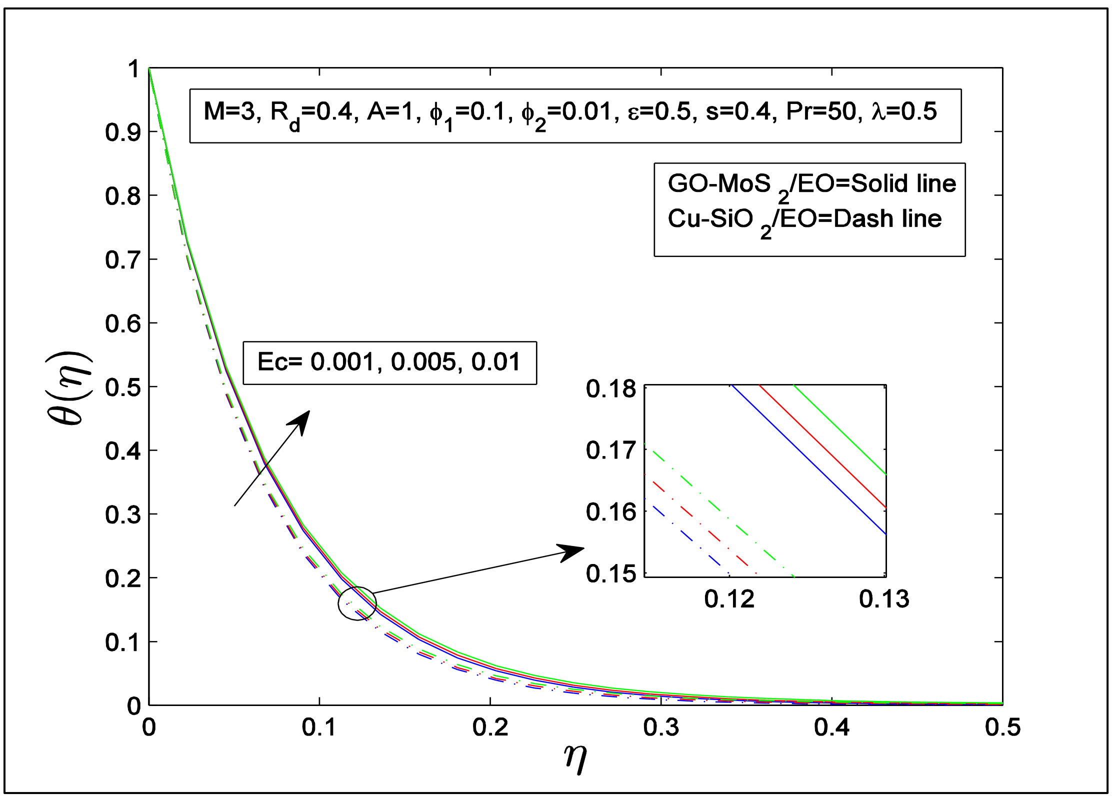

Figure 16. Temperature distribution for various values of Ec

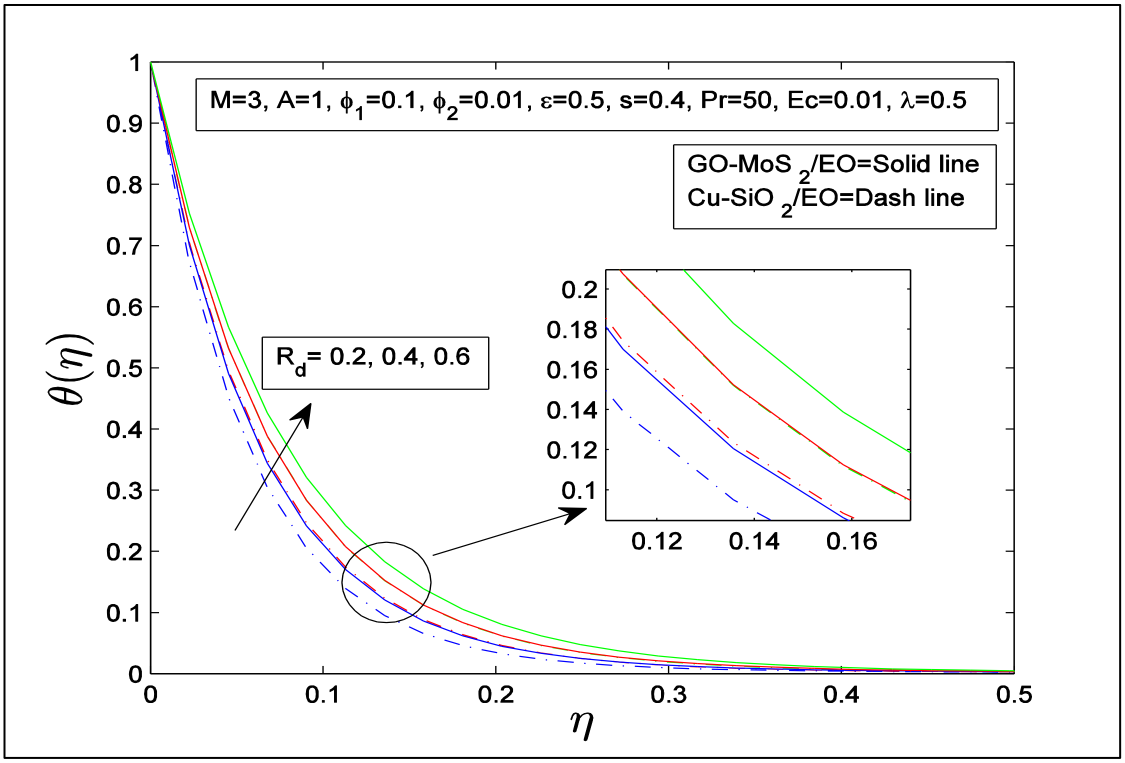

Figure 17. Temperature distribution for various values of R_d

Figures (16) and (17) visualize the modification in temperature profile $\theta(\eta)$, with a change in Eckert number Ec and radiation parameter R_d. An increment in both parameters produces a substantial enhancement in temperature. Eckert number features in the modified viscous dissipation term, $+\frac{\mu_{hnf}/\mu_f}{(\rho C_p)_{hnf}/(\rho C_p)_f} Ec\{f''(\eta)\}^2$ in Eqn. (8). Ec represents the relative contribution of kinetic energy expended as internal friction to the boundary layer enthalpy difference. It arises both in high speed and low velocity transport and is generated by molecular ballistic collisions in the nanofluid which create a heating effect. Since the overall kinetic energy in the flow is reduced, and transitions to thermal energy, temperatures are boosted. Strong viscous heating induces large elevations in thermal boundary layer thickness (Fig. 16). Markedly larger temperatures are associated with $\mathrm{GO-MoS_2}$/Engine oil hybrid nanofluid compared with $\mathrm{Cu-SiO_2}$/Engine oil, at any value of Eckert number. The radiative parameter, R_d (Fig. 17) arises only in the augmented thermal diffusion term, $\frac{1}{Pr\times\{(\rho C_p)_{hnf}/(\rho C_p)_f\}}\left\{\frac{K_{hnf}}{K_f}+\frac{4}{3}R_d\right\}\theta''(\eta)$, also in Eqn. (8). $R_d=\frac{4\sigma^* T_\infty^3}{K^* K_f}$ and is variously known as the Rosseland, Stark, or Boltzmann conduction-radiation parameter in heat transfer literature. This parameter in fact defines the relative contribution of thermal radiation heat transfer to thermal conduction heat transfer. For R_d = 0 radiation contribution vanishes. When R_d = both conduction and radiation contribute equally. For R_d < 1 thermal conduction dominates and for R_d> 1 thermal radiation dominates. The Rosseland diffusion model is confined to optically thick fluids (the general limit for optical thickness is around 5), this approach only simulates absorption and emission, not scattering of radiative energy. It is important to note that in the present nanofluid formulations, while absorption properties are assumed, thy are not explicitly addressed. Optical thickness and absorption coefficient quantify the degree to which a given medium inhibits the passage of thermal radiation. Radiative intensity is known to be depleted by an exponential factor when optical thickness is unity. Physically optical thickness is dependent on not only absorption coefficient, medium density but also propagation distance. Nevertheless, although more complex radiative formulations are available that may address these issues (and will be explored in future studies), the present simple flux model does manage to capture the thermal energizing behaviour of radiative heat flux, even with relatively weak values of R_d < 1. The strongest adjustment in temperatures is witnessed at intermediate distances from the wall and the free stream. Thermal boundary layer thickness is clearly accentuated with increment in radiative flux. As with earlier plots, $\mathrm{GO-MoS_2}$/Engine oil hybrid nanofluid demonstrates better thermal enhancement than $\mathrm{Cu-SiO_2}$/Engine oil.

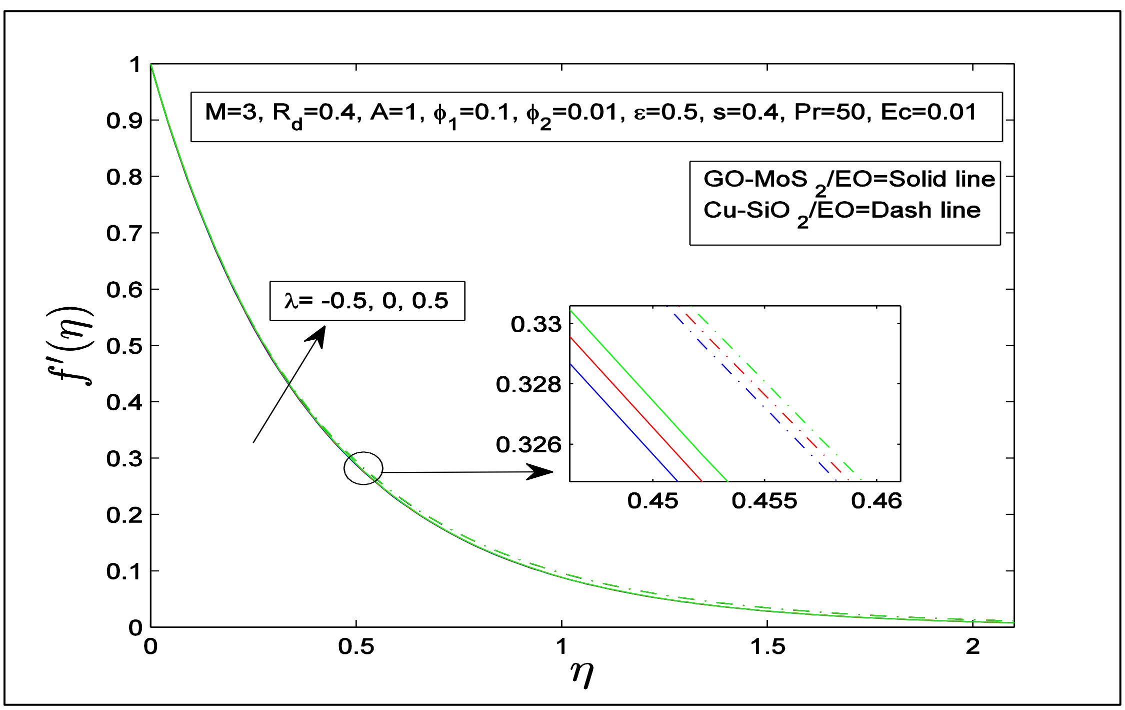

Figure 18. Velocity distribution for various values of λ

Figure (18) displays the impact of the thermal buoyancy parameter, λ, on the velocity profiles $f'(\eta)$ gets increased. $\lambda = \frac{Gr}{Re_x^2}$ and appears in a single term, $+\frac{(\rho\beta)_{hnf}/(\rho\beta)_f}{\rho_{hnf}/\rho_f}\lambda\theta(\eta)$, in the momentum eqn. (7). This couples very strongly the velocity and temperature fields and represents the natural convection effect. For forced convection $\lambda \to 0$. As λ increases positively the thermal buoyancy force contribution relative to resistive viscous force is elevated. Positive λ also implies that the thermal buoyancy force assists the inertial force in the free convection process. This mobilizes stronger convection currents and accelerates the boundary layer flow. However, for $\lambda < 0$, the thermal buoyancy force opposes the inertial force and this produces a damping effect. Momentum boundary layer thickness is therefore increased for $\lambda < 0$ whereas it is depleted with $\lambda > 0$. Furthermore, the nature of the thermal buoyancy can be exploited to manipulate velocity characteristics in the regime in combination with the type of hybrid nanofluid utilized for the nano-coating since $\mathrm{Cu-SiO_2/Engine\ oil}$ produces stronger flow acceleration than $\mathrm{GO-MoS_2/}$ $\mathrm{Engine\ oil}$.

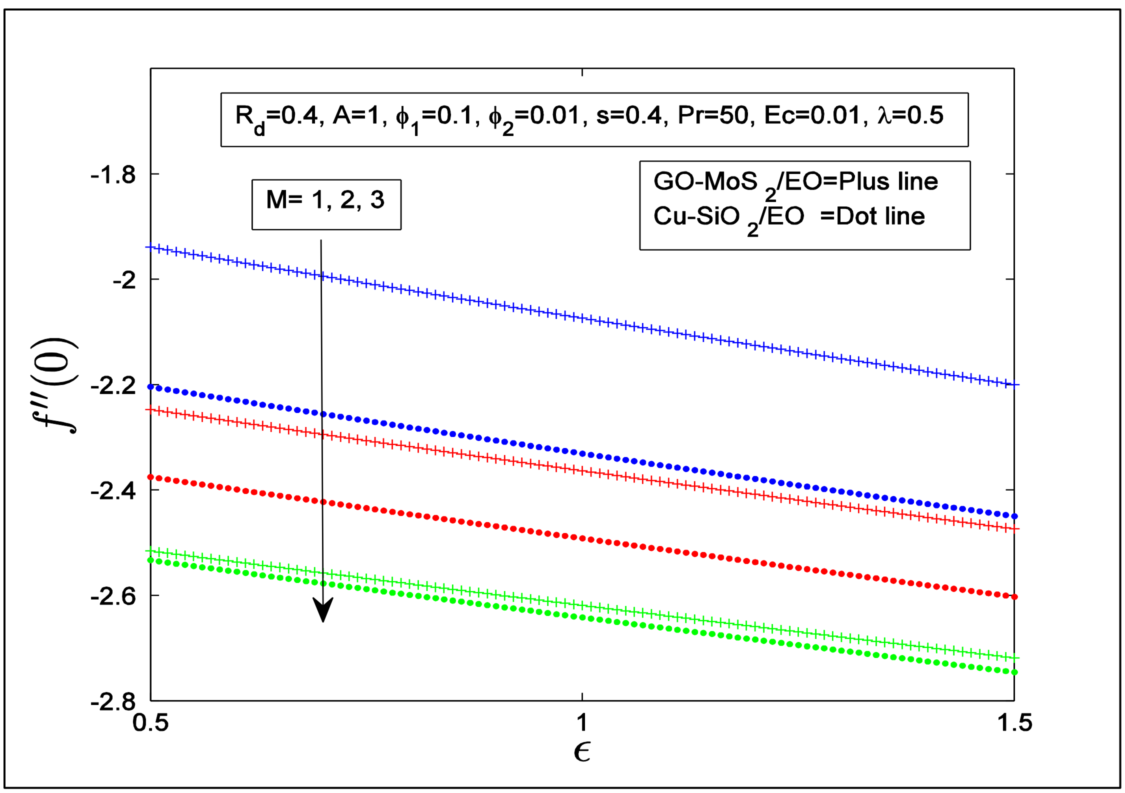

Figure 19. Variation of $f''(0)$ with ϵ for various values of M

Fig. 19 illustrates the impact of the inverse permeability parameter ϵ and the magnetic interaction parameter M, on skin friction coefficient. In figure (19), larger values of ϵ i. e. progressively lower permeability are observed to strongly reduce skin friction (a linear decay is computed). $\mathrm{GO}-\mathrm{MoS_2}$/Engine oil produces higher (more positive) skin friction coefficient values than $\mathrm{Cu}-\mathrm{SiO_2}$/Engine oil. Clearly lower permeability resists the percolation of both hybrid nanofluids and decelerates the flow. However, it is noteworthy that utilizing porous media is intrusive since the nanofluid is percolating the permeable material. This is classified as an intrusive technique in flow control in materials processing. However, via appropriate deployment of inert porous materials, with larger porosity (e. g. ceramic foams), chemical reactions and tortuosity effects may be mitigated. An increment in magnetic parameter M, is also found to suppress skin friction coefficient. The damping effect induced with a stronger external magnetic field is confirmed. Efficient flow regulation is therefore achieved in the nano-coating via this non-intrusive methodology. Attention has been confined her to static and transverse magnetic field. However, it is possible to modify the orientation of the applied field via a suitable circuit set up and study oblique magnetic field effects, a topic under consideration for future investigations. Also, the use of an alternating magnetic field (sinusoidal form) may also constitute an interesting refinement to the current analysis.

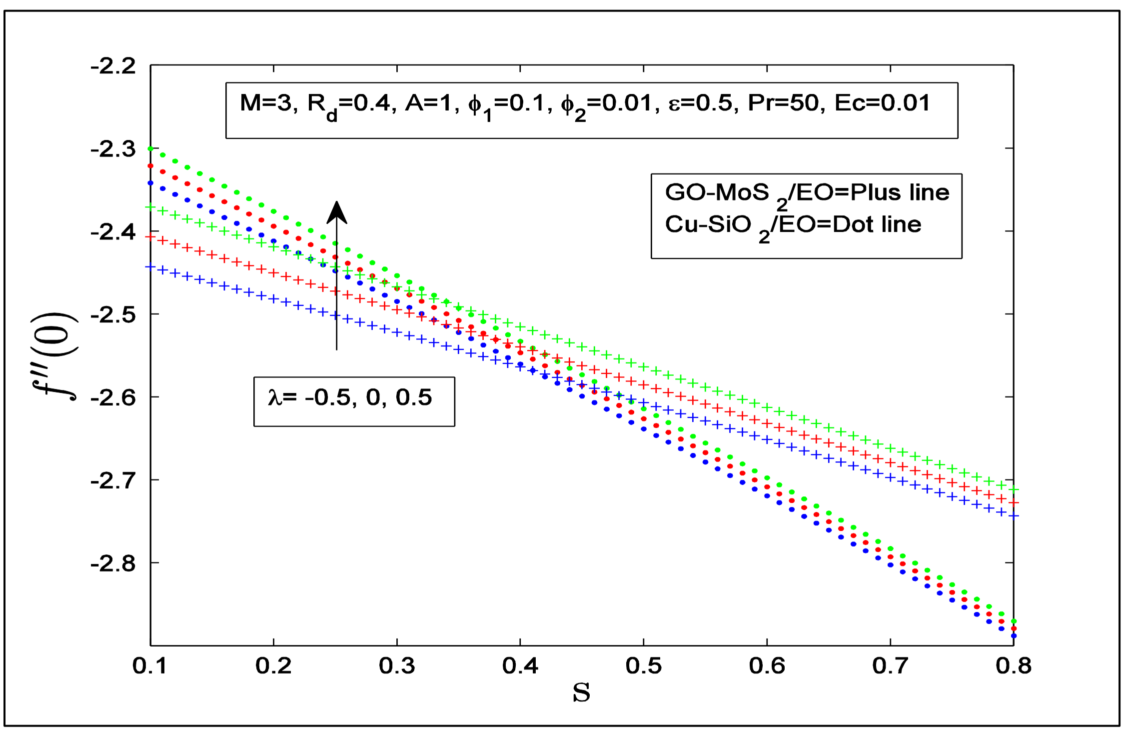

Figure 20. Variation of $f''(0)$ with s for various values of λ

In figure (20), the collective influence of wall mass flux (suction, s>0) and thermal buoyancy parameter, λ, on skin friction coefficient have been visualized. While larger suction clearly manifests in a sustained linear decay in skin friction, the response for the two hybrid nanofluids alters after a critical value of suction (s~0.4) is attained. Prior to this $\mathrm{Cu}-\mathrm{SiO_2}/\mathrm{Engine\ oil}$ attains higher (more-positive) skin friction coefficient than $\mathrm{GO}-\mathrm{MoS_2}/\mathrm{Engine\ oil}$ hybrid nanofluid. However, after s ~0.4, the response is reversed and $\mathrm{GO}-\mathrm{MoS_2}/\mathrm{Engine\ oil}$ is associated with higher skin friction values. The rate of descent in skin friction with increasing suction is generally sharper for the $\mathrm{GO}-\mathrm{MoS_2}/\mathrm{Engine\ oil}$ case. At any value of suction, negative thermal buoyancy parameter (λ<0) decreases skin friction whereas positive thermal buoyancy parameter ($\lambda > 0$) increases it. The forced convection case (λ=0) falls between these two other cases.

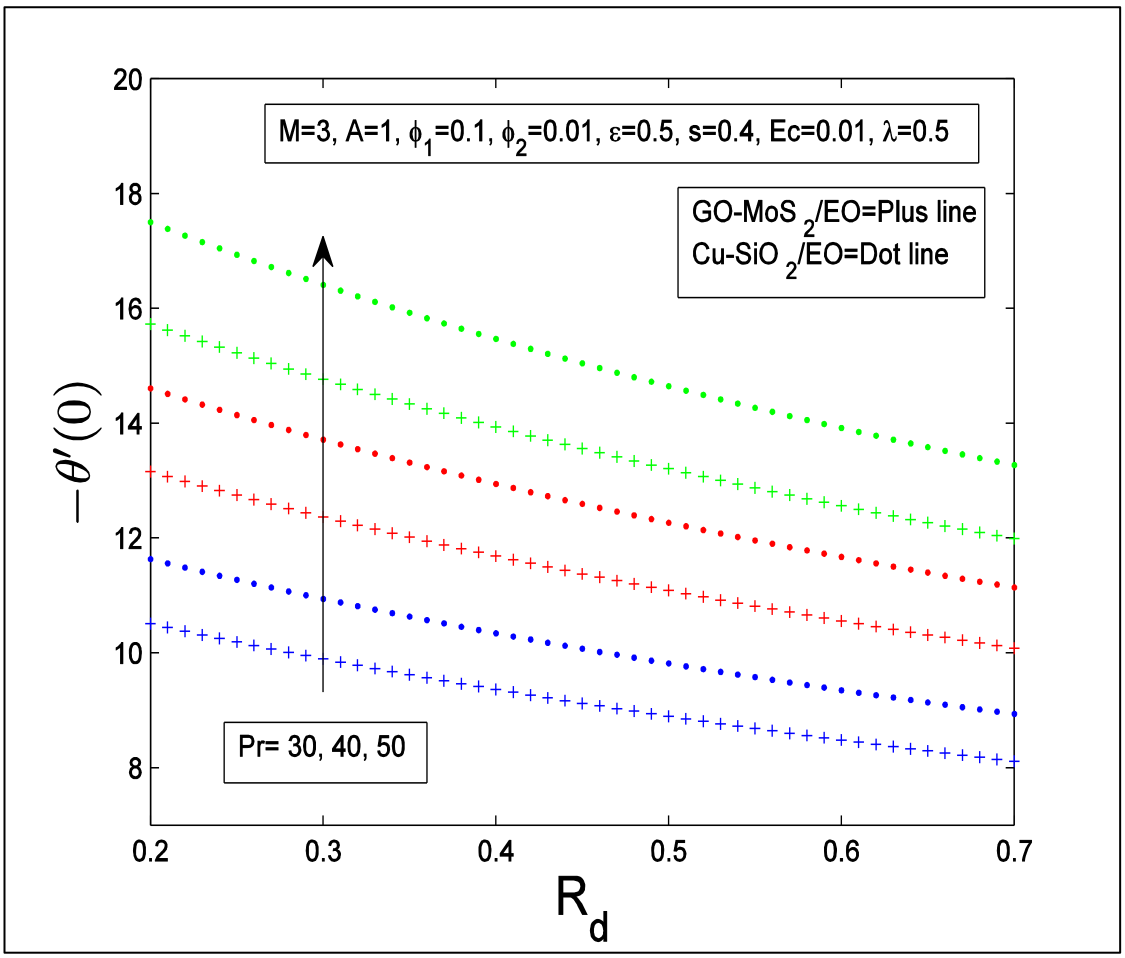

Figure 21. Variation of $-\theta'(0)$ with R_d for various values of Pr

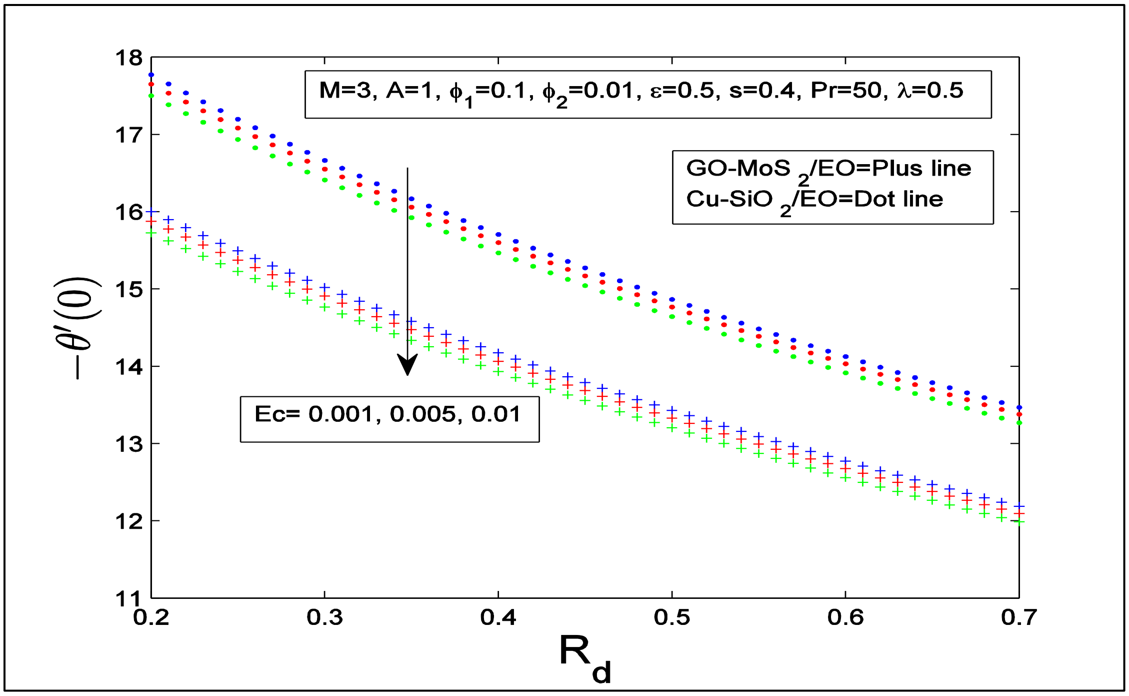

Figure 22. Variation of $-\theta'(0)$ with R_d for various values of Ec

Figs 21-22 show the combined impact of several parameters on local Nusselt number distribution. Fig. (21) shows that with increasing the radiation parameter R_d, the local Nusselt number is reduced. Since higher temperatures are produced in both hybrid nanofluids with stronger radiation flux, the net rate of heat transferred to the wall is diminished. This manifests in a plummet in Nusselt number magnitudes. $\mathrm{Cu-SiO_2/Engine\ oil}$ hybrid nanofluid therefore achieves higher Nusselt number than $\mathrm{GO-MoS_2/Engine\ oil}$ hybrid nanofluid, which is the opposite trend to that computed earlier in the temperature plots. It is further evident from figure (21) that local Nusselt number is increased with greater Prandtl number, which again is the contrary behaviour to that computed for the temperature distributions earlier. The lower thermal conductivity associated with higher Prandtl number cools the boundary layer. This results in an overall transit in thermal energy to the wall producing higher Nusselt numbers. In figure (22), local Nusselt number is likewise observed to decrease with increasing Eckert number. Since greater viscous dissipation is induced with increasing Ec values, temperatures are boosted due to the conversion of mechanical energy into heat. This results in a net migration of heat from the wall to the hybrid nanofluid. In other words, heat transferred from the nanofluid to the wall (sheet) is reduced producing lower Nusselt numbers. In fig 22 once again higher Nusselt numbers are computed for $\mathrm{Cu-SiO_2/Engine\ oil}$ hybrid nanofluid relative to the $\mathrm{GO-MoS_2/Engine\ oil}$ hybrid nanofluid.

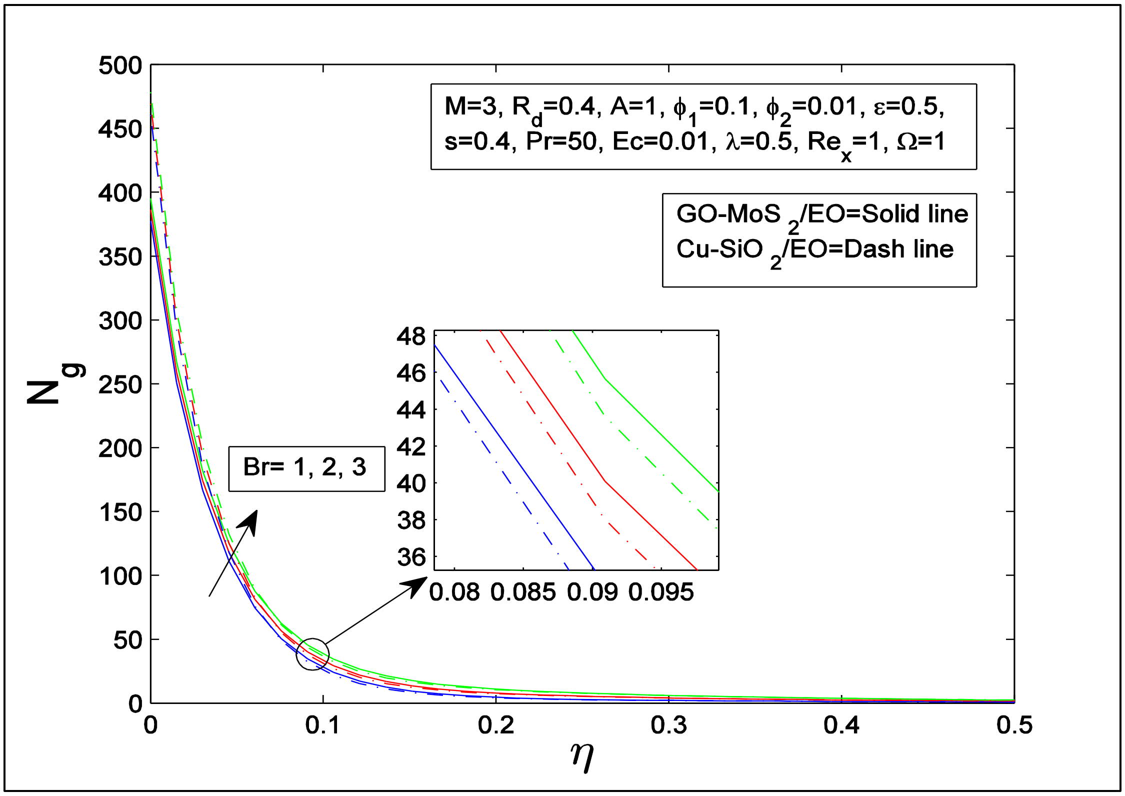

Figure 23. Variation of N_g for various Br

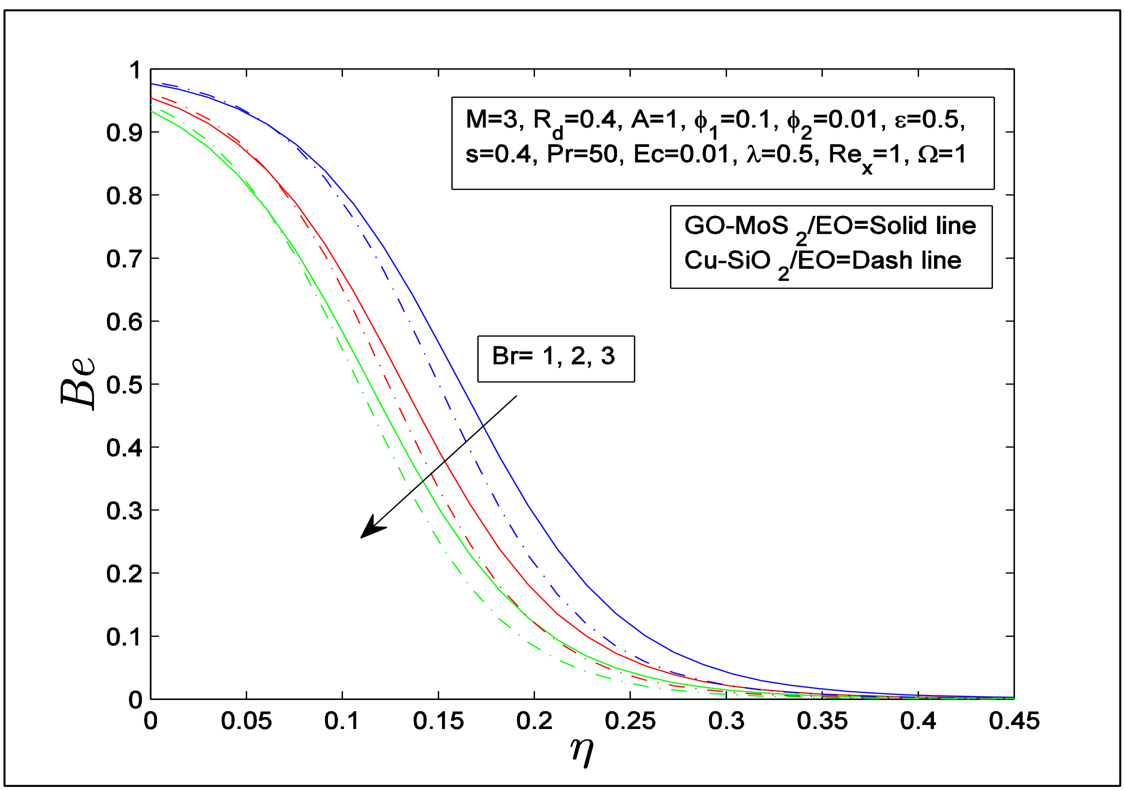

Figure 24. Variation of Be for various Br

In figures (23) and (24) display the influence of Brinkman number (Br) on entropy generation rate (N_g) and Bejan number (Be), respectively. Increasing Brinkman number generates an elevation in entropy generation rate (N_g) whereas it suppresses Bejan number (Be). Conventionally Brinkman number, $Br = \frac{\mu_f U_w^2}{K_f(T_w - T_\infty)}$ quantifies the relative significance of viscous heating to the conductive heat transfer. It is particularly important when a significant velocity change arises over short distances such as nano-coating processes. It also embodies the ratio of the heat generation by viscous forces to the heat transferred from the wall to the nanofluid. As elaborated earlier when $Be = 1$ this corresponds to the limit at which the irreversibility due to heat transfer dominates while $Be = 0$ corresponds to the opposite limit where the irreversibility is only due to fluid friction. With increasing Brinkman number, higher viscous heating generated in proximity to the wall boundary intensifies the difference between the nanofluid fluid temperature and the wall (sheet) temperature. The temperature gradient becomes steeper, indicating that there is an upsurge in heat transported from the wall to the fluid increases at higher Brinkman number. This leads to a boost in entropy generation rate (*Ng*). The contrary behaviour computed in Bejan number indicates that maximum entropy produced at the wall is mainly attributable to the fluid friction irreversibility and compensated by the heat transfer irreversibility. In both figures (23) and (24), $\mathrm{GO} - \mathrm{MoS_2/Engine\ oil}$ corresponds to higher entropy generation and Bejan number than $\mathrm{Cu} - \mathrm{SiO_2/Engine\ oil}$ hybrid nanofluid. The use of entropy generation minimization (EGM) clearly enables a clear picture of the relative contributions of viscous heating and thermal conduction to be quantified.

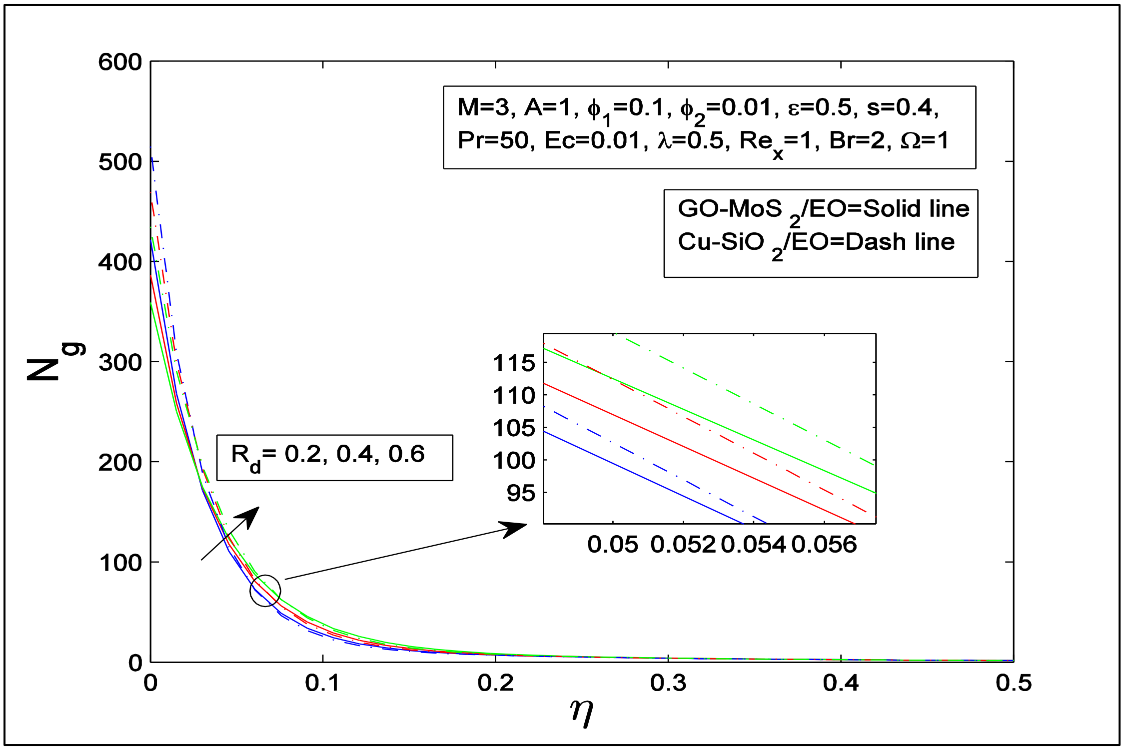

Figure 25. Variation of N_g for various R_d

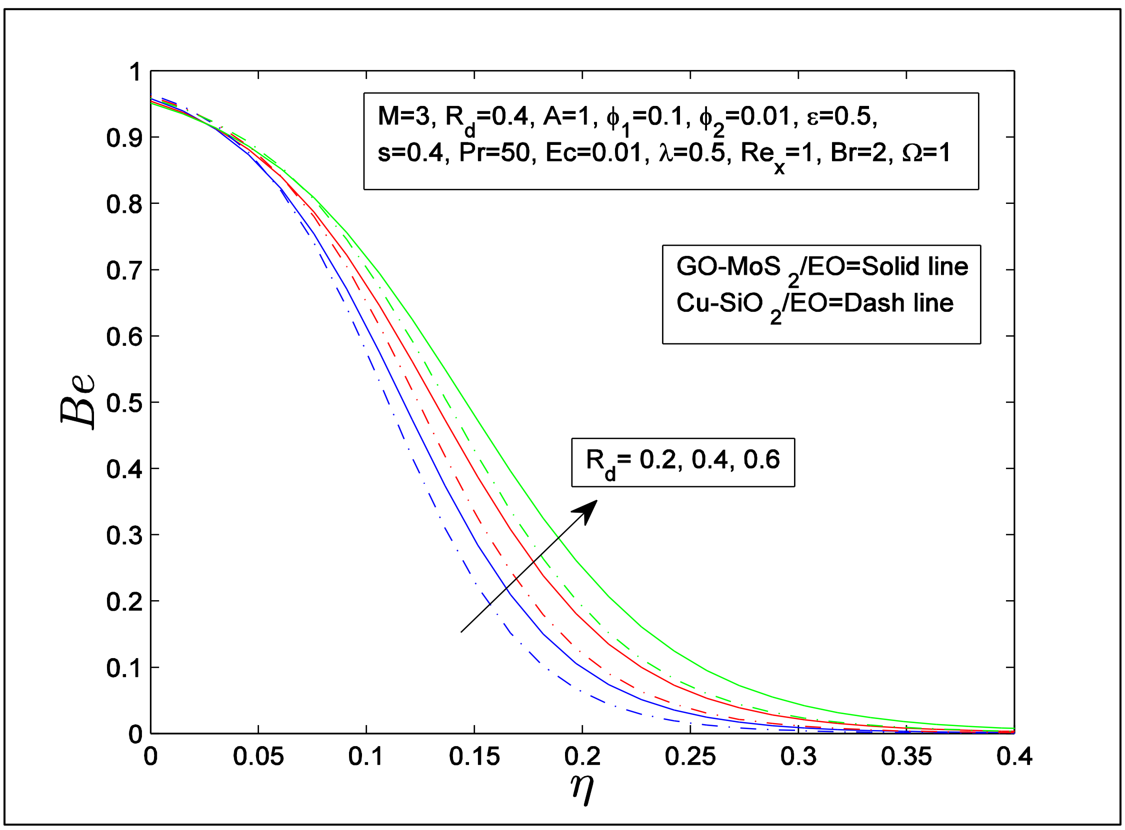

Figure 26. Variation of N_g for various R_d

Finally, in figures (25) and (26) the influence of radiation parameter (R_d) on entropy generation rate (N_g) and Bejan number (Be) is plotted. Increasing radiation parameter leads to an escalation in both entropy generation rate (N_g) and Bejan number (Be). With increasing radiation parameter (R_d), $\mathrm{GO}-\mathrm{MoS}_2$/Engine oil achieves lower entropy generation rate but a higher Bejan number than $\mathrm{Cu}-\mathrm{SiO}_2$/Engine oil hybrid nanofluid Radiative flux clearly induces significant changes in the entropy generation in the nano-coating regime. The inclusion of a radiative flux model is therefore justified since purely conductive-convective flow models will tend to produce erroneous estimates not only for temperature and Nusselt numbers (as computed earlier) but also entropy generation rate and Bejan number.

7. CONCLUSIONS

A neural network-based computation and entropy generation minimization (EGM) have been conducted for boundary layer hybrid magnetic nano-coating flow along a stretching surface to a porous medium with viscous heating. A Rosseland diffusion flux model has been employed for radiation heat transfer and Darcy's model has been used for the isotropic porous medium. Wall suction and injection have also been considered: 2 unitary nanofluids (Cu-engine oil and graphene oxide-engine oil) and 2 hybrid nanoparticle combinations i. e. graphite oxide (GO)-molybdenum disulfide (MoS_2) and copper (Cu)-silicon dioxide (SiO_2), both with engine oil as the base fluid, have been studied. The dimensional boundary layer model has been transformed via suitable scaling variables from a partial differential system into a dimensionless non-linear coupled ordinary differential system. The transformed boundary value problem has been solved computationally with the BVP4C subroutine in the symbolic software MATLAB. Plots have been produced for velocity, temperature, skin friction, Nusselt number, entropy generation rate, Bejan number, including mean squared errors, performance, training, error histogram, regression and fitting. Verification of the numerical methodology has been included with earlier studies from the literature. The computations have shown that:

(i) Hybrid nanofluid generally achieve improved heat transfer rates compared with unitary nanofluids.

(ii) The neural network optimization analysis deployed which incorporates Bayesian regularization as the training algorithm, has demonstrated that for the $\mathrm{Cu}-\mathrm{SiO_2/Engine}$ oil hybrid nanofluid regime, the mean square error is minimized at 678 epochs whereas it is computed at 404 epochs for the (GO)-molybdenum disulfide (MoS_2)/Engine oil case.

(iii) The Bejan entropy generation minimization (EGM) analysis shows that with increasing radiation parameter R_d, both entropy generation rate and Bejan number are increased, whereas with increasing Brinkman number Br only entropy generation rate is elevated whereas Bejan number is reduced.

(iv)With increasing values of nanoparticle solid volume fraction φ_2, magnetic parameter M, inverse permeability parameter ϵ, surface injection parameter $(s < 0)$, Eckert number Ec and radiation parameter R_d and with a decrement in suction parameter $(s > 0)$ and Prandtl number Pr, there is a significant boost in nanofluid temperature and thermal boundary layer thickness.

(v)With greater nanoparticle solid volume fraction φ_2, magnetic parameter M, inverse permeability parameter ϵ, suction parameter s and a reduction in thermal buoyancy parameter, λ, strong flow deceleration is induced, and momentum boundary layer thickness is increased.

(vi) Skin friction coefficient is substantially elevated with lower values of magnetic parameter M, inverse permeability parameter ϵ, suction parameter s and higher values of thermal buoyancy parameter, λ.

(vii) Nusselt number is reduced with greater radiation parameter R_d and Eckert number, *Ec*.

The present computations have identified some important characteristics of nanocoating flow processing using a variety of approaches. However, attention has been confined to Newtonian behaviour. Future work may consider a wide spectrum of non-Newtonian models including viscoplastic, viscoelastic and microstructural formulations and will be reported imminently. Additionally, some other pathways relevant to magnetic nanofluid coatings include Majeed *et al.* [77] considered entropy generation and thermal convective flow of magnetized hybrid nanofluid within a closed hexagonal domain containing a cylinder. Additionally, Majeed *et al.* [78] considered the integration of CFD simulations with ANN, utilizing CFD-generated datasets to optimize neuron count for improved accuracy in modeling incompressible flow around a cylinder. These aspects may also be addressed in the future.

CONFLICT OF INTEREST: None

ACKNOWLEDGEMENT: We are grateful to University of Dhaka and University Grants Commission of Bangladesh Grant 2022-2023 for providing the financial support for this work.

REFERENCES

1. H. Schlichting, *Boundary-layer Theory*, MacGraw-Hill, 6th edn (1979).

2. L. J. Crane, Flow past a stretching plate, *ZAMP*, vol. 21, no. 4, pp. 645–647, 1970.

3 H. T. Lin and Y. P. Shih, Buoyancy effects on the laminar boundary layer heat transfer along vertically moving cylinders, *Journal of the Chinese Institute of Engineers*, vol. 4, no.1, pp. 47–51, 1981.

4. R. Cortell, Viscous flow and heat transfer over a nonlinearly stretching sheet, *Applied Mathematics and Computation*, vol. 184, no. 2, pp. 864–873, 2007.

5. S. J. Weinstein and K. J. Ruschak, Coating flows, *Annual Review of Fluid Mechanics*, 36, 29-53, 2004.

6. H. I. Andersson and B. S. Dandapat, Flow of a power law fluid over a stretching sheet, *Stability and Applied Analysis of Continuous Media*, vol. 1, pp. 339–347, 1991.

7. P. S. Gupta and A. S. Gupta, Heat and mass transfer on a stretching sheet with suction and blowing, *The Canadian Journal of Chemical Engineering*, vol. 55, no. 6, pp. 744–746, 1977.

8. O. Anwar Bég, B. Vasu, Atul Kumar Ray, T.A. Bég, Ali Kadir, Henry J. Leonard and R.S.R. Gorla, Homotopy simulation of dissipative micropolar flow and heat transfer from a two-dimensional body with heat sink effect: applications in polymer coating, *Chem. Biochem. Eng. Quart.* 34 (4) 257–275, 2020.

9. A. Shahid, M. M. Bhatti, O. Anwar Bég and A. Kadir, Numerical study of radiative Maxwell viscoelastic magnetized flow from a stretching permeable sheet with the Cattaneo–Christov heat flux model, *Neural Computing and Applications*, 30, 3467–3478, 2018.

10. E. Magyari and B. Keller, Heat and mass transfer in the boundary layers on an exponentially stretching continuous surface, *Journal of Physics D*, vol. 32, no. 5, pp. 577–585, 1999.

11. A. Ishak, MHD boundary layer flow due to an exponentially stretching sheet with radiation effect, *Sains Malaysia*, vol. 40, no. 4, pp. 391–395, 2011.

12. Ghadimi A., Saidur R., Metselaar H, A review of nanofluid stability properties and characterization in stationary conditions, *International Journal of Heat and Mass Transfer*, vol. 54, no. 17-18, pp. 4051–4068, 2011.

13. S. U. S. Choi, Enhancing thermal conductivity of fluids with nanoparticles, *Proceedings of the ASME International Mechanical Engineering Congress and Exposition, San Francisco, USA*, vol. 66, pp. 99–105, 1995.

14. Giwa S.O., Adegoke K.A., Sharifpur M., Meyer J.P. Research trends in nanofluid and its applications: A bibliometric analysis. *Journal of Nanoparticle Research*, vol. 24, no. 63, pp. 1–22, 2022.

15. Meyer J.P., Adio S.A., Sharifpur M., Nwosu P.N., The viscosity of nanofluids: A review of the theoretical, empirical, and numerical models. *Heat Transfer Engineering*, vol. 37, no. 5, pp. 387–421, 2016.

16. O. Anwar Bég, Nonlinear multi-physical laminar nanofluid bioconvection flows: Models and computation, *A. Sohail, Z. Li (Eds.): Computational Approaches in Biomedical Nano-Engineering, Wiley, Chapter 5, pp. 113-145, 2018.*

17. A. V. Kuznetsov and D. A. Nield, Natural convective boundary layer flow of a nanofluid past a vertical plate, *International Journal of Thermal Sciences*, vol. 49, no. 2, pp. 243–247, 2010.

18. S. Özerinç, S. Kakaç, and A. G. YazIcIoğlu, Enhanced thermal conductivity of nanofluids: a state-of-the-art review, *Microfluidics and Nanofluidics*, vol. 8, no. 2, pp. 145–170, 2010.

19. X. Q. Wang and A. S. Mujumdar, A review on nanofluids—part I: theoretical and numerical investigations, *Brazilian Journal of Chemical Engineering*, vol. 25, no. 4, pp. 613–630, 2008.

20. Y. Li, J. Zhou, S. Tung, E. Schneider, and S. Xi, A review on development of nanofluid preparation and characterization, *Powder Technology*, vol. 196, no. 2, pp. 89–101, 2009.

21. Sarkar, J., Ghosh, P. and Adil, A review on hybrid nanofluids: recent research, development and applications, *Renewable and Sustainable Energy Reviews*, vol. 43, pp. 164-177, 2015.

22. K. Niihara, New design concept of structural ceramics/ceramic nanocomposites, *Nippon Seramikkusu Kyokai Gakujutsu Ronbunshi*, vol. 99, pp. 974–982, 1991.

23. S. Jana, A. Salehi-Khojin, and W. -H. Zhong, Enhancement of fluid thermal conductivity by the addition of single and hybrid nano-additives, *Thermochimica Acta*, vol. 462, no. 1-2, pp. 45–55, 2007.

24. S. Suresh, K. P. Venkitaraj, P. Selvakumar, and M. Chandrasekar, Synthesis of Al_2O_3 cu/water hybrid nanofluids using two step method and its thermo physical properties, *Colloids and Surfaces A: Physicochemical and Engineering Aspects*, vol. 388, no. 1-3, pp. 41–48, 2011.

25. G. G. Momin, Experimental investigation of mixed convection with water-Al_2O_3 & hybrid nanofluid in inclined tube for laminar flow, *International Journal of Scientific & Technology Research*, vol. 2, pp.195–202, 2013.

26. S. Suresh, K. P. Venkitaraj, P. Selvakumar, and M. Chandrasekar, Effect of Al_2O_3–cu/water hybrid nanofluid in heat transfer, Experimental Thermal and Fluid Science, vol. 38, pp. 54–60, 2012.

27. P.K. Pattnaik, S. R. Mishra, O. Anwar Bég, Umar F. Khan and J.C. Umavathi, Axisymmetric radiative titanium dioxide magnetic nanofluid flow on a stretching cylinder with homogeneous/heterogeneous reactions in Darcy-Forchheimer porous media: *intelligent nanocoating simulation, Materials Science and Engineering B* (2021). doi.org/10.1016/j.mseb.2021.115589 (26 pages).

28. Usman, M., Hamid, M., Zubair, T., Haq, R. U. & Wang, W. Cu- Al_2O_3/Water hybrid nanofluid through a permeable surface in the presence of nonlinear radiation and variable thermal conductivity via LSM. *International Journal of Heat and Mass Transfer*. vol. 126, pp. 1347–1356, 2018.

29. Nayak, M. K., Sher, N., Pandey, V. S., Hayat, Z. & Tripathi, D, 3D free convective MHD flow of nanofluid over permeable linear stretching sheet with thermal radiation. *Powder Technology*, vol. 315, pp. 205–215, 2017.

30. Khan, M. I., Hafeez, M. U., Hayat, T., Khan, M. I. & Alsaedi, A., Magneto rotating flow of hybrid nanofluid with entropy generation. *Computer Methods and Programs in Biomedicine,* vol. 183, 105093, 2020.

31. Reddy, J. V. R., Sugunamma, V., Sandeep, N. & Sulochana, Influence of chemical reaction, radiation and rotation on MHD nanofluid flow past a permeable flat plate in porous medium, *Journal of the Nigerian Mathematical Society*. vol. 35, pp. 48–65, 2016.

32. S.P. Samrat, C. Sulochana, G.P. Ashwinkumar, Impact of thermal radiation on an unsteady Casson nanofluid flow over a stretching surface, *International Journal of Applied and Computational Mathematics*, vol. 5, 31, 2019.

33. Iqbal, Z., Akbar, N. S., Azhar, E. & Maraj, E. N. Performance of hybrid nanofluid (Cu-CuO / water) on MHD rotating transport in oscillating vertical channel inspired by Hall current and thermal radiation. *Alexandria Engineering Journal*, vol. 57, pp. 1943–1954, 2018.

34. J. Prakash, Dharmendra Tripathi, Nevzat Akkurt and O. Anwar Bég, Tangent hyperbolic non-Newtonian radiative bioconvection nanofluid flow from a bi-directional stretching surface with electro-magneto-hydrodynamic, Joule heating and modified diffusion effects, *European Physical Journal Plus.*, 137: 472,(2022*. doi.org/10.1140/epjp/s13360-022-02613-x*

35. O. Anwar Bég, M.S. Khan, I. Karim, M.M. Alam and M. Ferdows, Explicit numerical study of unsteady hydromagnetic mixed convective nanofluid flow from an exponentially stretching sheet in porous media, *Applied Nanoscience, 4 (8) 943-957, 2014.*

36. Wang, C.Y., A fluid film sprayed on a three-dimensional stretching/shrinking sheet, *Fluid Dynamics Research*, vol. 43, no. 8, 2013.

37. M Ferdows, MS Khan, O. Anwar Bég, MAK Azad, MM Alam, Numerical study of transient magnetohydrodynamic radiative free convection nanofluid flow from a stretching permeable surface, *Proc. IMechE-Part E: J. Process Mechanical Engineering*, 228 (3) 181-196, 2014.

38. Mustafa, M., Mushtaq, A., Hayat, T. & Alsaedi, A, Radiation effects in three-dimensional flow over a bi-directional exponentially stretching sheet, *Journal of the Taiwan Institute of Chemical Engineers*, vol. 47, pp. 43-49, 2015.

39. M.J. Uddin, O. Anwar Bég and A.I. Ismail, Radiative-convective nanofluid flow past a stretching/shrinking sheet with slip effects, *AIAA J. Thermophysics Heat Transfer*, 29, 3, 513-523, 2015.
.
40. Grosan, T. and Pop, I., Flow and heat transfer over a permeable biaxial stretching/shrinking sheet in a nanofluid, *Neural Computing and Applications*, pp. 1-8, 2018.

41. A. Bejan, Entropy generation minimization: the new thermodynamics of finite size devices and finite-time processes, *Journal of Applied Physics*, vol. 79, pp. 1191–1218, 1996.

42. A. Bejan, Method of entropy generation minimization, or modeling and optimization based on combined heat transfer and thermodynamics, *R. Gen. Therm*., vol. 35, pp. 637–646, 1996.

43. A. Sciacovelli, V. Verda, E. Sciubba, Entropy generation analysis as a design tool—a review, *Renewable and Sustainable Energy Reviews*, vol. 43, pp. 1167–1181, 2015.

44. K. Manjunath, S.C. Kaushik, Second law thermodynamic study of heat exchangers: a review, *Renewable and Sustainable Energy Reviews*, vol. 40, pp. 348–374, 2014.

45. G. Janardhana Reddy, Mahesh Kumar and O. Anwar Bég, Effect of temperature dependent viscosity on entropy generation in transient viscoelastic polymeric fluid flow from an isothermal vertical plate, *Physica A - Statistical Mechanics and its Applications)*, 510, 426–445, 2018.

46. N. Gajjela, S. Jangili, J.R.V. Murthy and O. Anwar Bég, Mathematical modelling of entropy generation in magnetized micropolar flow between co-rotating cylinders with internal heat generation, *Alexandria Engineering J.*, 55, 1969-1982, 2016.

47. H. Thameem Basha, R. Sivaraj, V. R. Prasad, O. Anwar Bég, Entropy generation of tangent hyperbolic nanofluid flow over a circular cylinder in the presence of nonlinear Boussinesq approximation: A non-similar solution, *J. Thermal Analysis and Calorimetry*, 143, 2273–2289, 2021.

48. M.I. Khan , S. Sumaira , T. Hayat , M. Waqas , M.I. Khan , A. Alsaedi , Entropy gen- eration minimization and binary chemical reaction with Arrhenius activation energy in MHD radiative flow of nanomaterial, Journal of Molecular Liquids, vol. 259, pp. 274–283, 2018.

49. N. Shukla, Puneet Rana, O. Anwar Bég, A. Kadir and Bani Singh, Unsteady electromagnetic radiative nanofluid stagnation-point flow from a stretching sheet with chemically reactive

nanoparticles, Stefan blowing effect and entropy generation, *Proc. IMechE: Part N-Journal of Nanomaterials, Nanoengineering and Nanosystems,* 232, 69-82 2018.

50. A.S. Reddy, K. Govindarajulu, O. Anwar Bég and V.R. Prasad, Entropy generation on hydromagnetic oscillating flow of third grade nanofluid in a porous channel with Cattaneo-Christov heat flux, *Indian J. Chemical Technology,* 30, 9-22, 2023.
.
51. M. Ali Abbas, O. Anwar Bég, A. Zeeshan, A. Hobiny, M. M. Bhatti, Parametric analysis and minimization of entropy generation in bioinspired magnetized non-Newtonian nanofluid pumping using artificial neural networks and particle swarm optimization, *Thermal Science and Engineering Progress*, 2021. *doi.org/10.1016/j.tsep.2021.100930 (10 pages)*

52. Alizadeh R, Mohebbi Najm Abad J, Fattahi A, Alhajri E, Karimi N., Application of machine learning to investigation of heat and mass transfer over a cylinder surrounded by porous media—the radial basic function network. *Journal of Energy Research Technology*, vol. 142, 112109, 2020.

53. Abad JMN, Alizadeh R, Fattahi A, Doranehgard MH, Alhajri E, Karimi N., Analysis of transport processes in a reacting flow of hybrid nanofluid around a bluff-body embedded in porous media using artificial neural network and particle swarm optimization, *Journal of Molecular Liquids*, vol. 313, 113492, 2020.

54. Ahmad I, Zahid H, Ahmad F, Raja MAZ, Baleanu D., Design of computational intelligent procedure for thermal analysis of porous fin model, *Chinese Journal of Physics*, vol. 59, pp. 641–655, 2019.

55. Abdollahi A, Shams M, Optimization of heat transfer enhancement of nanofluid in a channel with winglet vortex generator, *Applied Thermal Engineering*, vol. 91, pp. 1116–1126, 2015.

56. Uysal C, Korkmaz ME, Estimation of entropy generation for Ag-MgO/water hybrid nanofluid flow through rectangular mini-channel by using artificial neural network, *Politeknik Dergisi*, vol. 22, no.1, pp. 41–51, 2019.

57. Saritha, M.; Joseph, K.P.; Mathew, A.T., Classification of MRI brain images using combined wavelet entropy-based spider web plots and probabilistic neural network, *Pattern Recognition Letters*, vol. 34, pp. 2151–2156, 2013.

58. Hoptroff, R.G. The principles and practice of time series forecasting and business modelling using neural nets, *Neural Computing & Applications*, vol. 1, pp. 59–66, 1993.

59. Patan, K., Neural network-based model predictive control: Fault tolerance and stability, *IEEE Transactions on Control Systems Technology*, vol. 23, pp. 1147–1155, 2014.

60. Maleque, K., Effects of binary chemical reaction and activation energy on MHD boundary layer heat and mass transfer flow with viscous dissipation and heat generation/absorption, *International Scholarly Research Notices*, vol. 2013, 284637, 2013.

61. Bhatti, M., Yousif, M.A., Mishra, S., Shahid, A., Simultaneous influence of thermo-diffusion and diffusion-thermo on non-Newtonian hyperbolic tangent magnetized nanofluid with Hall current through a nonlinear stretching surface, *Pramana*, vol. 93, pp. 1–10, 2019.

62. Devi, S.P.A. and Devi, S.S.U., Numerical investigation of hydromagnetic hybrid $Cu - Al_2O_3$ −water nanofluid flow over a permeable stretching sheet with suction, *International Journal of Nonlinear Sciences and Numerical Simulation*, vol. 17, no. 5, pp. 249-257, 2016.

63. Devi, S.S.U. and Devi, S.P.A., Numerical investigation of three-dimensional hybrid $Cu - Al_2O_3$ −water nanofluid flow over a stretching sheet with effecting Lorentz force subject to Newtonian heating, *Canadian Journal of Physics*, vol. 94, no. 5, pp. 490-496, 2016.

64. M. Khan, A. Rasheed, Slip velocity and temperature jump effects on molybdenum disulfide MoS2 and silicon oxide SiO_2 hybrid nanofluid near irregular 3D surface, *Alexandria Engineering Journal*, vol. 60, pp. 1689-1701, 2021.

65. Sohail, Ali, M. Ashraf, H. Khalifa, Fayza and Din, Analysis of pure nanofluid (GO/engine oil) and hybrid nanofluid (GO–Fe_3O_4 /engine oil): Novel thermal and magnetic features, *Nanotechnology Reviews*, vol. 11, pp. 2903–2915, 2022.

66. S. Sindhu and B.J. Gireesha, Entropy generation analysis of hybrid nanofluid in a microchannel with slip flow, convective boundary and nonlinear heat flux, *International Journal of Numerical Methods for Heat & Fluid Flow*, vol. 31, pp. 53-74, 2020.

67. D. Pal, S. Mondal & H. Mondol, Entropy generation on MHD Jeffrey nanofluid over a stretching sheet with nonlinear thermal radiation using spectral quasilinearisation method, *International Journal of Ambient Energy*, vol. 42, pp. 1712-1726, 2019.

68. L.F. Shampine, I. Gladwell, L. Shampine, S. Thompson, *Solving ODEs with MATLAB*, Cambridge University Press (2003).

69. S. Ahmad, K. Ali, K. Nisar, Features of Cu and TiO_2 in the flow of engine oil subject to thermal jump conditions, *Scientific Reports*, vol. 11, 19592, 2021.

70. M. Arif, P. Kumam, Dolat Khan, W. Watthayu, Thermal performance of GO-MoS_2/ engine oil as Maxwell hybrid nanofluid flow with heat transfer in oscillating vertical cylinder, *Case Studies in Thermal Engineering*, vol. 27, 101290, 2021.

71. D. Gamachu, W. Ibrahim, Entropy production on couple-stress hybrid nanofluid flow in a rocket engine nozzle with non-Fourier's and non-Fick's law, *Ain Shams Engineering Journal*, vol. 14, 101818, 2023.

72. W. Jamshed, Numerical investigation of MHD impact on Maxwell nanofluid, *International Communications in Heat and Mass Transfer*, vol. 120, 104973, 2021.

73. K.S. Nisar, W. Jamshed, Computational single phase comparative study of Williamson nanofluid in parabolic trough solar Collector via Keller box method, International Journal of Energy Research, vol. 45, pp. 10696-10718, 2021.

74. W. Jamshed, K. S. Nisar, R. W. Ibrahim, T. Mukhtar, V. Vijayakumar, F. Ahmad, Computational framework of Cattaneo-Christov heat flux effects on engine oil-based Williamson hybrid nanofluids: A thermal case study, *Case Studies in Thermal Engineering*, vol.26, 101179, 2021.

75. C.L. Tien and K. Vafai, Convective and radiative heat transfer in porous media, *Advances in Applied Mechanics, Editor(s): John W. Hutchinson, Theodore Y. Wu*, 27, 225-281 (1989).

76. Koch, C. C. *Nanostructured Materials: Processing, Properties and Applications*, William Andrew Publishing; 2nd edition, (2007).

77. A. H. Majeed, R. Mahmood, H. Shahzad, A. A. Pasha, N. Islam, M. M. Rahman, Numerical simulation of thermal flows and entropy generation of magnetized hybrid nanomaterials filled in a hexagonal cavity, *Case Studies in Thermal Engineering,* vol.39, 102293, 2022.

78. R. Mahmood, A. H. Majeed, H. Shahzad, I. Khan, Novel prediction of fluid forces on obstacle in a periodic flow regime using hybrid FEM-ANN simulations, *The European Physical Journal Plus,* vol.138, 741, 2023.